Available online at www.sciencedirect.com
ScienceDirect
Comput. Methods Appl. Mech. Engrg. 291 (2015) 146–172
Computer methods in applied mechanics and engineering
www.elsevier.com/locate/cma

An adaptive octree finite element method for PDEs posed on surfaces

Alexey Y. Chernyshenko[a], Maxim A. Olshanskii[b,*]

[a] *Institute of Numerical Mathematics, Russian Academy of Sciences, Moscow 119333, Russian Federation*
[b] *Department of Mathematics, University of Houston, Houston, TX 77204-3008, United States*

Received 18 August 2014; received in revised form 25 March 2015; accepted 30 March 2015
Available online 7 April 2015

Highlights

- We develop a second order accurate adaptive numerical method for PDEs posed on surfaces.
- The method does not fit a mesh or triangulates a surface. The surface may be given implicitly.
- No PDE extensions off the surface is needed. Only standard computational tools on bulk octree grids are required.
- The method enjoys rigorous error analysis. An error indicator is also introduced.

Abstract

The paper develops a finite element method for partial differential equations posed on hypersurfaces in $\mathbb{R}^N$, $N = 2, 3$. The method uses traces of bulk finite element functions on a surface embedded in a volumetric domain. The bulk finite element space is defined on an octree grid which is locally refined or coarsened depending on error indicators and estimated values of the surface curvatures. The cartesian structure of the bulk mesh leads to easy and efficient adaptation process, while the trace finite element method makes fitting the mesh to the surface unnecessary. The number of degrees of freedom involved in computations is consistent with the two-dimension nature of surface PDEs. No parametrization of the surface is required; it can be given implicitly by a level set function. In practice, a variant of the marching cubes method is used to recover the surface with the second order accuracy. We prove the optimal order of accuracy for the trace finite element method in H^1 and L^2 surface norms for a problem with smooth solution and quasi-uniform mesh refinement. Experiments with less regular problems demonstrate optimal convergence with respect to the number of degrees of freedom, if grid adaptation is based on an appropriate error indicator. The paper shows results of numerical experiments for a variety of geometries and problems, including advection–diffusion equations on surfaces. Analysis and numerical results of the paper suggest that combination of cartesian adaptive meshes and the unfitted (trace) finite elements provide simple, efficient, and reliable tool for numerical treatment of PDEs posed on surfaces.

Keywords: Surface; PDE; Finite elements; Traces; Unfitted grid; Octree grid

* Corresponding author.
E-mail address: molshan@math.uh.edu (M.A. Olshanskii).

http://dx.doi.org/10.1016/j.cma.2015.03.025
0045-7825/

1. Introduction

Partial differential equations posed on surfaces arise in mathematical models for many natural phenomena: diffusion along grain boundaries [1], lipid interactions in biomembranes [2], and transport of surfactants on multiphase flow interfaces [3], as well as in many engineering and bioscience applications: vector field visualization [4], textures synthesis [5], brain warping [6], fluids in lungs [7] among others. Thus, recently there has been a significant increase of interest in developing and analyzing numerical methods for PDEs on surfaces.

One natural approach to solving PDEs on surfaces numerically is based on surface triangulation. In this class of methods, one typically assumes that a parametrization of a surface is given and the surface is approximated by a family of consistent regular triangulations. It is common to assume that all nodes of the triangulations lie on the surface. The analysis of a finite element method based on surface triangulations was first done in [8]. To avoid surface triangulation and remeshing (if the surface evolves), another approach was taken in [9]: It was proposed to extend a partial differential equation from the surface to a set of positive Lebesgue measure in $\mathbb{R}^N$. The resulting PDE is then solved in one dimension higher, but can be solved on a mesh that is unaligned to the surface. A surface is allowed to be defined implicitly as a zero set of a given level set function. However, the resulting bulk elliptic or parabolic equations are degenerate, with no diffusion acting in the direction normal to the surface. Versions of the method, where only an h-narrow band around the surface is used to define a finite element method, were studied in [10,11]. An overview of finite element methods for surface PDEs and more references can be found in the recent review paper [12].

Another unfitted finite element method for equations posed on surfaces was introduced in [13,14]. That method does not use an extension of the surface partial differential equation. It is instead based on a restriction (trace) of the outer finite element spaces to a surface. The trace finite element method does not need parametrization or fitting a mesh to the surface and avoids some well known pitfalls of PDE-extension based methods related to the bulk equation degeneracy and numerical boundary conditions. Since only those bulk elements are involved in computations which are intersected by a surface, the number of active degrees of freedom is consistent with the dimensionality of the surface problem. The trace finite element method is also very natural approach when one needs to solve a system of partial differential equations that couples bulk domain effects with interface (or surface) effects, the situation which occurs in a number of applications [15,16]. Therefore, recently several authors developed the trace finite element method in various directions: In [17–20] the method was extended and analyzed for the case of evolving surfaces; Papers [21,22] considered surface-bulk coupled problems, and [23] treated singular-perturbed surface advection–diffusion equation; An analysis of higher order trace finite elements was given in [24]; A posteriori estimates and adaptivity were studied in [25]; Versions of the method with improved algebraic properties were introduced in [26,10]. All these studies considered continuous piecewise polynomial (typically P_1) bulk finite elements with respect to a regular tetrahedral subdivision of a volumetric domain or a regular triangulation in 2D case.

In the present paper, the trace finite element method is developed for octree bulk meshes. The cartesian structure and embedded hierarchy of octree grids makes mesh adaptation, reconstruction and data access fast and easy, which is not always the case for tetrahedral meshes. For these reasons, octree meshes became a common tool in image processing, the visualization of amorphous medium, free surface and multi-phase flows computations and other applications where non-trivial geometries occur, see, for example, [27–32]. Thus, employing octree grids for numerical solution of PDEs on surfaces one benefits from their local adaptation properties in the case fine surface structures or solution with a singularity. Moreover, the resulting tool for solving surface PDEs is ready for coupling with many of existing octree-based methods (not restricted to finite element methods) for solving bulk problems. Some of these octree-based solvers are parts of the publicly available software, e.g., [33,34]. One intrinsic property of octree grids, however, is only the first order approximation of curved geometries. It appears that the trace finite element method is the right tool to deal with this potential shortcoming. We shall see that a surface may cut the octree mesh in an arbitrary way. The finite element method is unfitted and uses a second order surface recovery with a variant of the marching cubes algorithm [35]. As a formal demonstration of the method accuracy, we prove the $O(h)$ error estimate in the $H^1(\Gamma)$-norm and the $O(h^2)$ error estimate in the $L^2(\Gamma)$-norm on a smooth closed surface Γ. Here h is the maximum side length among all cubes intersected by the recovered (discrete) surface. To access the local error, we introduce an error indicator based on elementwise residual and surface curvature. A grid adaptation strategy based on this indicator leads to optimal convergence of numerical solution with respect to the number of degrees of freedom.

In the paper, we consider regular Laplace–Beltrami type problems as well as singular-perturbed advection–diffusion equations on surfaces. The latter case is of interest for a number of applications such as the transport of

surfactants along fluidic interfaces or a pollutant transport in fractured porous media. For the advection dominated problem we consider a stabilized variant of the trace finite element method as well as layer fitted meshes. The remainder of the paper is organized as follows. Section 2 sets up a problem. In Section 3, we introduce a finite element method. Analysis of the finite element method is presented in Section 4. It includes a well-posedness result, a priori and a posteriori error estimates. Section 5 collects the result of several numerical experiments. Finally, Section 6 contains some closing remarks.

2. Problem formulation

Let Ω be an open domain in $\mathbb{R}^3$ and Γ be a connected C^3 compact hyper-surface contained in Ω. For a sufficiently smooth function $g : \Omega \to \mathbb{R}$ the tangential derivative on Γ is defined by

$$\nabla_\Gamma g = \nabla g - (\nabla g \cdot \mathbf{n})\mathbf{n}, \tag{1}$$

where $\mathbf{n}$ denotes the unit normal to Γ. Denote by $\mathrm{div}_\Gamma = \nabla_\Gamma \cdot$ the surface divergence operator and by $\Delta_\Gamma = \nabla_\Gamma \cdot \nabla_\Gamma$ the Laplace–Beltrami operator on Γ. The simplest elliptic PDE on Γ is the classical Laplace–Beltrami equation

$$-\Delta_\Gamma u = f \quad \text{on } \Gamma, \text{ with } \int_\Gamma f \,\mathrm{d}\mathbf{s} = 0. \tag{2}$$

Although, (2) is an interesting problem arising in many applications, we shall consider a slightly more general problem on Γ. To motivate it, consider $\mathbf{w} : \Omega \to \mathbb{R}^3$, a given velocity field in Ω. If the surface Γ evolves with a normal velocity of $\mathbf{w} \cdot \mathbf{n}$ (e.g., Γ is passively advected by the velocity field $\mathbf{w}$), then the conservation of a scalar quantity u with a diffusive flux on $\Gamma(t)$ leads to the surface PDE, see, e.g., [12]:

$$\dot{u} + (\mathrm{div}_\Gamma \mathbf{w})u - \varepsilon \Delta_\Gamma u = 0 \quad \text{on } \Gamma(t), \tag{3}$$

where $\dot{u}$ denotes the advective material derivative, $\varepsilon > 0$ is the diffusion coefficient. If we assume $\mathbf{w} \cdot \mathbf{n} = 0$, i.e. the advection velocity is everywhere tangential to the surface, and the surface is steady in the geometric sense, then the surface advection–diffusion equation takes the form:

$$u_t + \mathbf{w} \cdot \nabla_\Gamma u + (\mathrm{div}_\Gamma \mathbf{w})u - \varepsilon \Delta_\Gamma u = 0 \quad \text{on } \Gamma. \tag{4}$$

Although the methodology of the paper is applied to the parabolic equations (4), we shall present the method and analysis for the stationary problem:

$$-\varepsilon \Delta_\Gamma u + \mathbf{w} \cdot \nabla_\Gamma u + (c + \mathrm{div}_\Gamma \mathbf{w})\, u = f \quad \text{on } \Gamma, \tag{5}$$

with $f \in L^2(\Gamma)$ and $c = c(\mathbf{x}) \in L^\infty(\Gamma)$. If $\mathbf{w} = 0$ and $c = 0$, we recover the classical Laplace–Beltrami problem (2). Otherwise we assume $\mathbf{w} \in H^{1,\infty}(\Gamma)$.

We need the following identity for integration by parts over Γ:

$$\int_\Gamma q(\mathrm{div}_\Gamma \mathbf{f}) + \mathbf{f} \cdot \nabla_\Gamma q \,\mathrm{d}\mathbf{s} = \int_\Gamma \kappa(\mathbf{f} \cdot \mathbf{n}) q \,\mathrm{d}\mathbf{s} \tag{6}$$

for smooth q and vector field $\mathbf{f}$, where $\kappa = \mathrm{div}_\Gamma \mathbf{n}$ is the (doubled) surface mean curvature. Applying (6) and $\mathbf{w} \cdot \mathbf{n} = 0$ one finds the equality

$$\int_\Gamma (\mathbf{w} \cdot \nabla_\Gamma u) v \,\mathrm{d}\mathbf{s} = -\int_\Gamma (\mathbf{w} \cdot \nabla_\Gamma v) u \,\mathrm{d}\mathbf{s} - \int_\Gamma (\mathrm{div}_\Gamma \mathbf{w})\, uv \,\mathrm{d}\mathbf{s}.$$

Integrating (5) over Γ and applying the above identity with $v = 1$, one finds that for $c = 0$ the source term in (5) should satisfy the zero mean constraint $\int_\Gamma f \,\mathrm{d}\mathbf{s} = 0$.

Introduce the bilinear form and the functional:

$$a(u, v) := \int_\Gamma \varepsilon \nabla_\Gamma u \cdot \nabla_\Gamma v - (\mathbf{w} \cdot \nabla_\Gamma v)u + c\, uv \,\mathrm{d}\mathbf{s},$$
$$f(v) := \int_\Gamma f v \,\mathrm{d}\mathbf{s}.$$

The weak formulation of (5) is as follows: Find $u \in V$ such that

$$a(u, v) = f(v) \quad \forall v \in V, \tag{7}$$

with

$$V = \begin{cases} \left\{ v \in H^1(\Gamma) \mid \int_\Gamma v \, \mathrm{d}\mathbf{s} = 0 \right\} & \text{if } c + \mathrm{div}_\Gamma \mathbf{w} = 0, \\ H^1(\Gamma) & \text{otherwise.} \end{cases}$$

For functions satisfying zero integral mean condition, the following Poincare's inequality holds:

$$\|v\|^2_{L^2(\Gamma)} \le C_P \|\nabla_\Gamma v\|^2_{L^2(\Gamma)} \quad \forall\, v \in V, \text{ s.t. } \int_\Gamma v \, \mathrm{d}\mathbf{s} = 0. \tag{8}$$

We shall assume

$$\begin{aligned} &\varepsilon C_P^{-1} - \sup_{\mathbf{x}\in\Gamma} |\mathrm{div}_\Gamma \mathbf{w}(\mathbf{x})| \ge c_0 > 0 \quad \text{if } c + \mathrm{div}_\Gamma \mathbf{w} = 0, \\ &c + \frac{1}{2}\mathrm{div}_\Gamma \mathbf{w} \ge c_0 > 0 \text{ on } \Gamma \qquad \text{otherwise.} \end{aligned} \tag{9}$$

If a time stepping scheme is used for (4) and c is proportional to the reciprocal of the time step, then the assumption is not restrictive.

The Lax–Milgram lemma and (8) immediately yield the well-posedness result for (7). A higher smoothness of the solution follows from a regularity result for the Laplace–Beltrami equation in [36].

Proposition 2.1. *Assume (9), then there exists a unique solution of (7), satisfying*

$$\frac{c_0}{2}\|u\|^2_{L^2(\Gamma)} + \varepsilon\|\nabla_\Gamma u\|^2_{L^2(\Gamma)} \le 2c_0^{-1}\|f\|^2_{L^2(\Gamma)} \tag{10}$$

and

$$\|u\|^2_{H^2(\Gamma)} \le C_2 \|f\|^2_{L^2(\Gamma)},$$

with a constant C_2 depending on ε, $\mathbf{w}$, c_0, and Γ.

3. The trace finite element method

In this section we review the trace FEM. The method developed in this section is an extension of the trace FEM introduced in [13].

3.1. The idea of the method

Assume we are given a polyhedral subdivision $\mathcal{T}_h$ of the bulk domain Ω and V_h is a $H^1(\Omega)$ conforming finite element space. Consider all traces of functions from V_h on Γ and denote the resulting space of surface functions by V_h^Γ. Now one substitutes V by V_h^Γ in the weak formulation (7) to obtain a finite element formulation. If Γ is given implicitly or no parametrization of Γ is known, a problem of integration of finite element functions over Γ arises. Hence in practice, Γ in the finite element formulation is replaced by an approximate ("discrete") surface Γ_h such that integration over Γ_h is feasible. For example, Γ_h is piecewise polygonal. Trace space for V_h is now defined over Γ_h rather than Γ and problem data is extended from Γ to Γ_h. Substituting Γ by Γ_h introduces a geometric error in the method that has to be quantified. It is remarkable, however, that a suitable Γ_h can be easily constructed for an implicitly given surface without any knowledge of the surface parametrization. Moreover, in some applications Γ is not known, and Γ_h is recovered from a solution to an (discretized) equation. The trace finite element method is perfectly suited for such a situation.

It is clear from this general description that both Γ and Γ_h may cut the bulk mesh in an arbitrary way. So the trace finite element method can be related to the family of unfitted finite element methods, well developed for equations posed in bulk domains, such as XFEM or cut-FEM. To build a basis or a frame in V_h^Γ, one may consider traces of

basis functions from V_h on Γ_h. It is also clear that only those bulk basis functions should be considered that have their support intersected by Γ_h.

Further in the paper, we study the method if $\mathcal{T}_h$ is a cubic octree mesh, V_h is a space of piecewise trilinear continuous finite elements, and Γ_h is reconstructed by a variant of marching cubes method from a piecewise trilinear interpolant to a level set function of Γ.

3.2. The method

Consider an octree cubic mesh $\mathcal{T}_h$ covering the bulk domain Ω. We assume that the mesh is gradely refined, i.e. the sizes of two neighboring cubes differ at most by a factor of 2. Such octree grids are also known as balanced. The method applies for unbalanced octrees, but in our analysis and experiments we use balanced grids.

Denoted by Γ_h a given polygonal approximation of Γ. We assume that Γ_h is a $C^{0,1}$ surface without boundary and Γ_h can be partitioned in planar triangular segments:

$$\Gamma_h = \bigcup_{T\in\mathcal{F}_h} T, \tag{11}$$

where $\mathcal{F}_h$ is the set of all triangular segments T. Without loss of generality we assume that for any $T \in \mathcal{F}_h$ there is only *one* cube $S_T \in \mathcal{T}_h$ such that $T \subset S_T$ (if T lies on a side shared by two cubes, any of these two cubes can be chosen as S_T).

In practice, we construct Γ_h as follows. Let ϕ_h be a piecewise trilinear continuous function with respect to the octree grid $\mathcal{T}_h$ and consider its zero level set

$$\widetilde{\Gamma}_h := \{\mathbf{x} \in \Omega \,:\, \phi_h(\mathbf{x}) = 0\}.$$

We assume that $\widetilde{\Gamma}_h$ is an approximation to Γ. This is a reasonable assumption if ϕ_h is an interpolant to ϕ, a level set function of Γ; one example of ϕ is the signed distance function for Γ. To define ϕ_h one only should be able to prescribe in each node an approximate distance to Γ. Alternatively, in some applications, ϕ_h is recovered from a solution of a discrete indicator function equation (e.g. in the level set or the volume of fluid methods), without any direct knowledge of Γ.

Once ϕ_h is known, we recover Γ_h by the cubical marching squares method from [37] (a variant of the very well-known marching cubes method). The method provides a triangulation of $\widetilde{\Gamma}_h$ within each cube such that the global triangulation is continuous, the number of triangles within each cube is finite and bounded by a constant independent of $\widetilde{\Gamma}_h$ and a number of refinement levels. Moreover, the vertices of triangles from $\mathcal{F}_h$ are lying on $\widetilde{\Gamma}_h$.

An illustration of a bulk mesh and a surface triangulation is given in Fig. 1. The mesh shown in this figure was obtained by representing a torus Γ implicitly by its signed distance function, constructing the piecewise trilinear continuous interpolant of this distance function and then applying the cubical marching squares method for reconstructing Γ_h from the zero level of this interpolant.

Note that the resulting triangulation $\mathcal{F}_h$ is *not* necessarily regular, i.e. elements from T may have very small internal angles and the size of neighboring triangles can vary strongly, cf. Fig. 1 (right). Thus, Γ_h is not a "triangulation of Γ" in the usual sense (an $O(h^2)$ approximation of Γ, consisting of regular triangles). The surface triangulation $\mathcal{F}_h$ is used only to define quadratures in the finite element method below, while approximation properties of the method, as we shall see, depend on the volumetric octree mesh.

The surface finite element space is *the space of traces on Γ_h of all piecewise trilinear continuous functions with respect to the outer triangulation $\mathcal{T}_h$*. This can be formally defined as follows.

Consider the volumetric finite element space of all piecewise trilinear continuous functions with respect to the bulk octree mesh $\mathcal{T}_h$:

$$V_h := \{v_h \in C(\Omega) \mid v|_S \in Q_1 \;\; \forall\, S \in \mathcal{T}_h\}, \quad \text{with } Q_1 = \operatorname{span}\{1, x_1, x_2, x_3, x_1x_2, x_1x_3, x_2x_3, x_1x_2x_3\}. \tag{12}$$

V_h induces the following space on Γ_h:

$$V_h^\Gamma := \{\psi_h \in H^1(\Gamma_h) \mid \exists\, v_h \in V_h \text{ such that } \psi_h = v_h|_{\Gamma_h}\}. \tag{13}$$

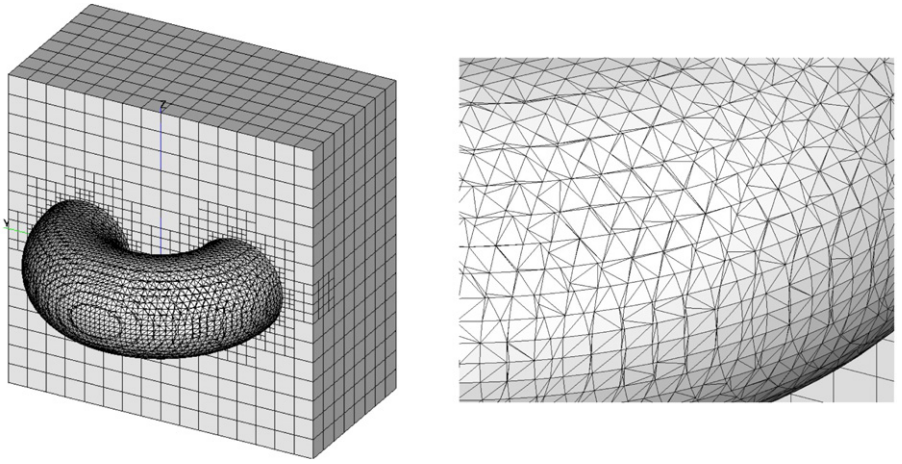

Fig. 1. Left: A cutaway of a bulk domain shows the bulk octree mesh three times refined towards the surface and the resulting approximate surface Γ_h for the part of a torus. Right: The zoom-in of the resulting surface triangulation. The triangulation does not satisfy a minimal angle condition.

Given the surface finite element space V_h^Γ, the finite element discretization of (5) is as follows: Find $u_h \in V_h^\Gamma$ such that

$$\varepsilon \int_{\Gamma_h} \nabla_{\Gamma_h} u_h \cdot \nabla_{\Gamma_h} v_h \; - (\mathbf{w}_h \cdot \nabla_{\Gamma_h} v_h) u_h + c_h \, u_h v_h \, \mathrm{d}\mathbf{s}_h = \int_{\Gamma_h} f_h v_h \, \mathrm{d}\mathbf{s}_h \tag{14}$$

for all $v_h \in V_h^\Gamma$. Here $\mathbf{w}_h$, c_h and f_h are some approximations of the problem data on Γ_h. A well-posedness result for (14) will be proved in the next section.

3.3. Variants of the method

Here we discuss several extensions of the trace finite element method (14), which can be advantageous in some situations. One obvious update of the method is the following one. Define a subdomain ω_h of Ω consisting only of those end-level cubic cells that contain Γ_h:

$$\omega_h = \bigcup_{T \in \mathcal{F}_h} S_T . \tag{15}$$

For the outer finite element space, instead of piecewise trilinear continuous functions in Ω, consider all such function restricted to ω_h:

$$V_h^\omega := \{ v_h \in C(\omega_h) \mid v|_S \in Q_1 \;\; \forall \, S \in \mathcal{T}_h \}.$$

Further, define the space of traces of functions from V_h^ω on Γ_h:

$$V_h^{\omega,\Gamma} := \{ \psi_h \in H^1(\Gamma_h) \mid \exists \, v_h \in V_h^\omega \text{ such that } \; \psi_h = v_h|_{\Gamma_h} \}.$$

It is clear that $V_h^\Gamma \subset V_h^{\omega,\Gamma}$. When the grid is locally refined, the dimension of the space $V_h^{\omega,\Gamma}$ can be larger for the following reason: The inter-element continuity of bulk finite element functions imposes algebraic constraints in hanging nodes. For the space $V_h^{\omega,\Gamma}$ such constraints should be imposed only for hanging nodes shared by two cubic cells from ω_h, but not for hanging nodes lying on the boundary of ω_h, which are now available for extra degrees of freedom.

We performed numerical experiments with the trace finite element space from (13) and observed optimal convergence behavior with respect to the number of degrees of freedom (cf. Section 5). We expect that the method with $V_h^{\omega,\Gamma}$ instead of V_h^Γ behaves similarly.

Furthermore, one may relax the continuity assumption for the bulk finite element functions in ω_h and consider a discontinuous Galerkin finite element method. This is an interesting (and natural in some sense) alternative for an octree based finite element method, which we plan to study elsewhere.

As usual with transport-diffusion problems, the advection terms can be written in several equivalent ways, leading, however, to different discretizations. For example, instead of $-(\mathbf{w}_h \cdot \nabla_{\Gamma_h} v_h)u_h$ one may choose the 'skew-symmetric' variant

$$\frac{1}{2}\int_{\Gamma_h} (\mathbf{w}_h \cdot \nabla_{\Gamma_h} u_h)v_h \; - (\mathbf{w}_h \cdot \nabla_{\Gamma_h} v_h)u_h + (\operatorname{div}_{\Gamma_h} \mathbf{w}_h)\, u_h v_h \,\mathrm{d}\mathbf{s}_h.$$

We shall analyze the 'conservative' formulation (14), since it avoids the surface divergence of $\mathbf{w}_h$. Our motivation is that for a polygonal surface reconstruction the term $\operatorname{div}_{\Gamma_h}\mathbf{w}_h$ leads to the consistency error of the method of order $O(h)$, if $\mathbf{w}_h$ is a smooth extension of $\mathbf{w}$ from Γ, and hence the observed asymptotic convergence of the method is at most $O(h)$. For the 'conservative' form we are able to prove $O(h^2)$ accuracy of the method.

Below we discuss a few more developments of the trace finite element method known from the literature.

3.3.1. Full gradient method

The "full gradient" variant of the trace finite element method was suggested in [10] and studied in [10,24]. The modification is aimed on improving algebraic properties of the stiffness matrix of the method. The rationality behind the full gradient method is clear from the following observation. For solution u of (5), denote by u^e its normal extension to an arbitrary small neighborhood $\mathcal{O}(\Gamma)$ of Γ, i.e., u^e is constant along normal directions to Γ. Note that $\nabla_\Gamma u = \nabla u^e$ and so u^e satisfies the identity (5) with surface gradients (in the diffusion term) replaced by full gradients:

$$\int_\Gamma \varepsilon \nabla u^e \cdot \nabla v \; - (\mathbf{w} \cdot \nabla_\Gamma v)u^e + c\, u^e v \,\mathrm{d}\mathbf{s} = \int_\Gamma f v \,\mathrm{d}\mathbf{s}$$

for all v sufficiently smooth in $\mathcal{O}(\Gamma)$ (v is not necessarily constant along normals). This identity shows that the following finite element formulation is consistent: Find $u_h \in V_h$ satisfying

$$\int_{\Gamma_h} \varepsilon \nabla u_h \cdot \nabla v_h \; - (\mathbf{w}_h \cdot \nabla_{\Gamma_h} v_h)u_h + c_h\, u_h v_h \,\mathrm{d}\mathbf{s}_h = \int_{\Gamma_h} f_h v_h \,\mathrm{d}\mathbf{s}_h \tag{16}$$

for all $v_h \in V_h$.

The full-gradient method (16) uses the bulk finite element space V_h instead of the surface finite element space V_h^Γ in (14). However, practical implementation of both methods uses the frame of all bulk finite element nodal basis functions $\phi_i \in V_h$ such that $\operatorname{supp}(\phi_i) \cap \Gamma_h \neq \emptyset$. Hence the active degrees of freedom in both methods are the same. The stiffness matrices are, however, different. For the case of the Laplace–Beltrami problem and a regular quasi-uniform tetrahedral grid, results in [10,24] show that the conditioning of the (diagonally scaled) stiffness matrix of the full gradient method substantially improves over the conditioning of the matrix for (14), for the expense of a slight deterioration of the accuracy of the method.

3.3.2. SUPG stabilized method

Similar to the plain Galerkin finite element for advection–diffusion equations the method (14) is prone to instability unless mesh is sufficiently fine such that the mesh Peclet number is less than one.

In [23], a SUPG type stabilized trace finite element method was introduced and analyzed for P_1 continuous bulk finite elements. The stabilized formulation reads: Find $u_h \in V_h^\Gamma$ such that

$$\begin{aligned}
&\int_{\Gamma_h} \varepsilon \nabla_{\Gamma_h} u_h \cdot \nabla_{\Gamma_h} v_h \; - (\mathbf{w}_h \cdot \nabla_{\Gamma_h} v_h)u_h + c_h\, u_h v_h \,\mathrm{d}\mathbf{s}_h \\
&\quad + \sum_{T\in\mathcal{F}_h} \delta_T \int_T (-\varepsilon \Delta_{\Gamma_h} u + \mathbf{w}_h \cdot \nabla_{\Gamma_h} u + (c_h + \operatorname{div}_{\Gamma_h}\mathbf{w}_h)\, u)\, \mathbf{w}_h \cdot \nabla_{\Gamma_h} v \,\mathrm{d}\mathbf{s}_h \\
&= \int_{\Gamma_h} f_h v \,\mathrm{d}\mathbf{s}_h + \sum_{T\in\mathcal{F}_h} \delta_T \int_T f_h (\mathbf{w}_h \cdot \nabla_{\Gamma_h} v) \,\mathrm{d}\mathbf{s}_h \quad \forall v_h \in V_h^\Gamma.
\end{aligned} \tag{17}$$

The stabilization parameter δ_T depends on $T \subset S_T$. The side length of the cubic cell S_T is denoted by h_{S_T}. Let $\mathsf{Pe}_T := \frac{h_{S_T}\|\mathbf{w}_h\|_{L^\infty(T)}}{2\varepsilon}$ be the cell Peclet number. We take

$$\widetilde{\delta_T} = \begin{cases} \dfrac{\delta_0 h_{S_T}}{\|\mathbf{w}_h\|_{L^\infty(T)}} & \text{if } \mathsf{Pe}_T > 1, \\ \dfrac{\delta_1 h_{S_T}^2}{\varepsilon} & \text{if } \mathsf{Pe}_T \le 1, \end{cases} \quad \text{and} \quad \delta_T = \min\{\widetilde{\delta_T}, c^{-1}\}, \tag{18}$$

with some given positive constants $\delta_0, \delta_1 \ge 0$.

3.3.3. Gradient-jump stabilized method

Another way of improving algebraic properties of the trace finite element method was suggested in [26]. In that paper, the authors introduced the term

$$J(u, v) = \sum_{F \in \omega_h^F} \sigma_F \int_{\partial F} [\![\mathbf{n}_F \cdot \nabla u]\!][\![\mathbf{n}_F \cdot \nabla v]\!],$$

with $\sigma_E = 0(1)$. Here ω_h^F denotes the set of all internal interfaces between cubic cells in ω_h, $\mathbf{n}_F$ is the normal vector for interface F, and $[\![\mathbf{n}_F \cdot \nabla u]\!]$ denotes the jump of the normal derivative of u across F. Now, the edge-stabilized trace finite element reads: Find $u_h \in V_h$ such that

$$\varepsilon \int_{\Gamma_h} \nabla_{\Gamma_h} u_h \cdot \nabla_{\Gamma_h} v_h \; - (\mathbf{w}_h \cdot \nabla_{\Gamma_h} v_h) u_h + c_h \, u_h v_h \, \mathrm{d}\mathbf{s}_h + J(u_h, v_h) = \int_{\Gamma_h} f_h v_h \, \mathrm{d}\mathbf{s}_h \tag{19}$$

for all $v_h \in V_h$.

For P_1 continuous bulk finite element methods on quasi-uniform regular tetrahedral meshes and the Laplace–Beltrami equation, the paper [26] shows the optimal orders of convergence of the trace finite element method (19) and improved algebraic properties of the stiffness matrix.

In this paper, we consider the trace finite element in (14), its full-gradient variant in (16), and the SUPG stabilized version (17) for the case of convection-dominated equations. We are not studying the edge stabilized version here.

4. Well-posedness and error analysis of the trace FEM

In this section, we state a well-posedness result for (14). Further, an error analysis of the trace method is presented for a regular problem (we assume ε is not too small). In particular, we shall prove optimal order of convergence of the method in H^1 and L^2 surface norms. The analysis can be extended to the full-gradient and the SUPG stabilized formulations following the arguments of [24] and [23], respectively. However, in this paper we restrict ourselves to the original formulation (14).

Let $\{\mathcal{T}_h\}_{h>0}$ be a family of octree meshes covering the domain Ω. Parameter h denotes the maximum size of a cubic cell from $\mathcal{T}_h$. For the sake of analysis, we assume that the maximum number of local refinement levels is bounded from above independently of h. Further, we need some more notations and definitions.

4.1. Preliminaries

For a given octree mesh $\mathcal{T}_h$ let Ψ_h be the set of all nodal basis functions of the bulk finite element space V_h. Here and further denote by Ω_h the union of all supports of nodal basis functions intersected by Γ_h:

$$\Omega_h = \bigcup_{\psi \in \Psi_h} \{\mathrm{supp}(\psi) \mid \mathrm{supp}(\psi) \cap \Gamma_h \neq \emptyset\}.$$

For the surface Γ, we define its h-neighborhood:

$$U_h := \{\mathbf{x} \in \mathbb{R}^3 \mid \mathrm{dist}(\mathbf{x}, \Gamma) < \tilde{c}\, h\}, \tag{20}$$

and assume that $\tilde{c}$ is sufficiently large and h is sufficiently small such that $\Omega_h \subset U_h \subset \Omega$ and

$$\tilde{c}\, h < \left(\max_{i=1,2} \|\kappa_i\|_{L^\infty(\Gamma)} \right)^{-1} \tag{21}$$

holds, with κ_i being the principal curvatures of Γ.

Let $d : U_h \to \mathbb{R}$ be the signed distance function. Thus Γ is the zero level set of d and $\Gamma \in C^3 \;\Rightarrow\; d \in C^3(U_h)$. We assume $d < 0$ in the interior of Γ and $d > 0$ in the exterior and define $\mathbf{n}(\mathbf{x}) := \nabla d(\mathbf{x})$ for all $\mathbf{x} \in U_h$. Hence, $\mathbf{n}$ is the normal vector on Γ and $|\mathbf{n}(\mathbf{x})| = 1$ for all $\mathbf{x} \in U_h$. The Hessian of d is denoted by

$$\mathbf{H}(\mathbf{x}) := \nabla^2 d(\mathbf{x}) \in \mathbb{R}^{3\times 3}, \quad \mathbf{x} \in U_h.$$

The eigenvalues of $\mathbf{H}(\mathbf{x})$ are denoted by $\kappa_1(\mathbf{x})$, $\kappa_2(\mathbf{x})$, and 0. For $\mathbf{x} \in \Gamma$ the eigenvalues κ_i, $i = 1, 2$, are the principal curvatures. For each $\mathbf{x} \in U_h$, define the projection $\mathbf{p} : U_h \to \Gamma$ by

$$\mathbf{p}(\mathbf{x}) = \mathbf{x} - d(\mathbf{x})\mathbf{n}(\mathbf{x}).$$

Due to the assumption (21), the decomposition $\mathbf{x} = \mathbf{p}(\mathbf{x}) + d(\mathbf{x})\mathbf{n}(\mathbf{x})$ is unique. We need the orthogonal projector

$$\mathbf{P}(\mathbf{x}) := \mathbf{I} - \mathbf{n}(\mathbf{x})\mathbf{n}(\mathbf{x})^T, \quad \text{for } \mathbf{x} \in U_h.$$

The tangential derivative can be written as $\nabla_\Gamma g(\mathbf{x}) = \mathbf{P}\nabla g(\mathbf{x})$ for $\mathbf{x} \in \Gamma$. One can verify that for this projection and for the Hessian $\mathbf{H}$ the relation $\mathbf{HP} = \mathbf{PH} = \mathbf{H}$ holds. Similarly, define

$$\mathbf{P}_h(\mathbf{x}) := \mathbf{I} - \mathbf{n}_h(\mathbf{x})\mathbf{n}_h(\mathbf{x})^T, \quad \text{for } \mathbf{x} \in \Gamma_h,\ \mathbf{x} \text{ is not on an edge},$$

where $\mathbf{n}_h$ is the unit (outward pointing) normal at $\mathbf{x} \in \Gamma_h$. The tangential derivative along Γ_h is given by $\nabla_{\Gamma_h} g(\mathbf{x}) = \mathbf{P}_h(\mathbf{x})\nabla g(\mathbf{x})$.

Assume the following estimates on how well Γ_h approximates Γ:

$$\text{ess sup}_{\mathbf{x}\in\Gamma_h} |d(\mathbf{x})| \le c_1 h^2, \tag{22}$$

$$\text{ess sup}_{\mathbf{x}\in\Gamma_h} |\mathbf{n}(\mathbf{x}) - \mathbf{n}_h(\mathbf{x})| \le c_2 h, \tag{23}$$

with constants c_1, c_2 independent of h. The assumption is reasonable if Γ is defined as the zero level of a (locally) smooth level set function ϕ and Γ_h is reconstructed as described in the previous section from the zero level set of $\phi_h \in V_h$, where ϕ_h interpolates ϕ and it holds

$$\|\phi - \phi_h\|_{L^\infty(U_h)} + h\|\nabla(\phi - \phi_h)\|_{L^\infty(U_h)} \le c\, h^2.$$

In the remainder, $A \lesssim B$ means $A \le c\, B$ for some positive constant c independent of h.

For $\mathbf{x} \in \Gamma_h$, define $\mu_h(\mathbf{x}) = (1 - d(\mathbf{x})\kappa_1(\mathbf{x}))(1 - d(\mathbf{x})\kappa_2(\mathbf{x}))\mathbf{n}^T(\mathbf{x})\mathbf{n}_h(\mathbf{x})$. The surface measures $\mathrm{d}\mathbf{s}$ and $\mathrm{d}\mathbf{s}_h$ on Γ and Γ_h, respectively, are related by

$$\mu_h(\mathbf{x})\mathrm{d}\mathbf{s}_h(\mathbf{x}) = \mathrm{d}\mathbf{s}(\mathbf{p}(\mathbf{x})), \quad \mathbf{x} \in \Gamma_h. \tag{24}$$

The assumptions (22) and (23) imply that

$$\text{ess sup}_{\mathbf{x}\in\Gamma_h} (1 - \mu_h) \lesssim h^2, \tag{25}$$

cf. (3.37) in [13]. The solution of (5) and its data are defined on Γ, while the finite element method is defined on Γ_h. Hence, we need a suitable extension of a function from Γ to its neighborhood. For a function v on Γ we define

$$v^e(\mathbf{x}) := v(\mathbf{p}(\mathbf{x})) \quad \text{for all } \mathbf{x} \in U_h.$$

The following formula for this lifting function are known (cf. section 2.3 in [38]):

$$\nabla u^e(\mathbf{x}) = (\mathbf{I} - d(\mathbf{x})\mathbf{H})\nabla_\Gamma u(\mathbf{p}(\mathbf{x})) \quad \text{in } U_h, \tag{26}$$

$$\nabla_{\Gamma_h} u^e(\mathbf{x}) = \mathbf{P}_h(\mathbf{x})(\mathbf{I} - d(\mathbf{x})\mathbf{H})\nabla_\Gamma u(\mathbf{p}(\mathbf{x})) \quad \text{a.e. on } \Gamma_h, \tag{27}$$

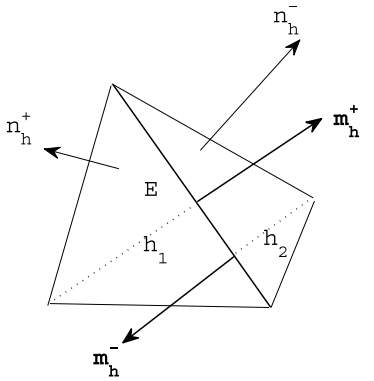

Fig. 2. Two neighboring surface triangles may belong to two different planes and so two tangential normals $\mathbf{m}_h^+$ and $\mathbf{m}_h^-$ to the edge E are not necessarily collinear.

with $\mathbf{H} = \mathbf{H}(\mathbf{x})$. By direct computation one derives the relation

$$\begin{aligned}\nabla^2 u^e(\mathbf{x}) \;=\; & (\mathbf{P} - d(\mathbf{x})\mathbf{H})\nabla^2 u(\mathbf{p}(\mathbf{x}))(\mathbf{P} - d(\mathbf{x})\mathbf{H}) - (n^T \nabla u(\mathbf{p}(\mathbf{x})))\mathbf{H} \\ & - (\mathbf{H}\nabla u(\mathbf{p}(\mathbf{x})))\mathbf{n}^T - \mathbf{n}(\mathbf{H}\nabla u(\mathbf{p}(\mathbf{x})))^T - d\nabla\mathbf{H} : \nabla u(\mathbf{p}(\mathbf{x})).\end{aligned} \tag{28}$$

For sufficiently smooth u and $|\mu| \le 2$, using this relation one obtains the estimate

$$|D^\mu u^e(\mathbf{x})| \lesssim \left(\sum_{|\mu|=2} |D^\mu_\Gamma u(\mathbf{p}(\mathbf{x}))| + |\nabla_\Gamma u(\mathbf{p}(\mathbf{x}))| \right) \quad \text{in } U_h, \tag{29}$$

(see also Lemma 3 in [8]). This further leads to (cf. Lemma 3.2 in [13]):

$$\|D^\mu u^e\|_{L^2(U_h)} \lesssim \sqrt{h}\|u\|_{H^2(\Gamma)}, \quad |\mu| \le 2. \tag{30}$$

For the analysis, we shall assume that $\mathbf{w}_h$, c_h and f_h are defined as the extensions of $\mathbf{w}$, c, and f, respectively, along normals to Γ, i.e. it holds

$$\mathbf{w}_h = \mathbf{w}^e, \qquad c_h = c^e, \quad \text{and} \quad f_h = f^e \quad \text{on } \Gamma_h. \tag{31}$$

4.2. Well-posedness

We need some further notations. For each $T \in \mathcal{F}_h$, denote by $\mathbf{m}_h|_E$ the outer normal to an edge E in the plane which contains element T. For curved geometries, "tangential" normal vectors to E from two different sides are not necessarily collinear, cf. Fig. 2. Let $[\![\mathbf{m}_h]\!]|_E = \mathbf{m}_h^+ + \mathbf{m}_h^-$ be the jump of two outward normals to the edge E. For a 'usual' planar case, this jump is zero. Over Γ_h, these jumps produce additional consistency term in the integration by parts formula:

$$\begin{aligned}-\int_{\Gamma_h} (\mathbf{w}_h \cdot \nabla_{\Gamma_h} v_h) u_h \, \mathrm{d}\mathbf{s}_h \;=\; & \frac{1}{2}\int_{\Gamma_h} (\mathbf{w}_h \cdot \nabla_{\Gamma_h} u_h) v_h - (\mathbf{w}_h \cdot \nabla_\Gamma v_h) u_h + (\mathrm{div}_{\Gamma_h} \mathbf{w}_h) u_h v_h \, \mathrm{d}\mathbf{s}_h \\ & - \frac{1}{4}\sum_{T\in\mathcal{F}_h} \int_{\partial T} (\mathbf{w}_h \cdot [\![\mathbf{m}_h]\!]) u_h v_h \, \mathrm{d}\mathbf{r}.\end{aligned} \tag{32}$$

We introduce the notation for the finite element bilinear form and the functional:

$$a_h(u, v) := \varepsilon \int_{\Gamma_h} \nabla_{\Gamma_h} u \cdot \nabla_{\Gamma_h} v \, - (\mathbf{w}_h \cdot \nabla_{\Gamma_h} v) u + c_h \, uv \, \mathrm{d}\mathbf{s}_h, \quad f_h(v) := \int_{\Gamma_h} f_h v \, \mathrm{d}\mathbf{s}_h.$$

The following result is now straightforward.

Proposition 4.1. *If one assumes*

$$\int_{\Gamma_h}\left(c_h+\frac{1}{2}\mathrm{div}_{\Gamma_h}\mathbf{w}_h\right)v_h^2\,\mathrm{d}\mathbf{s}_h-\frac{1}{4}\sum_{T\in\mathcal{F}_h}\int_{\partial T}(\mathbf{w}_h\cdot[\![\mathbf{m}_h]\!])v_h^2\,\mathrm{d}\mathbf{r}\geq c_0\|v_h\|^2_{L^2(\Gamma_h)},\quad \textit{for all } v_h\in V_h^{\Gamma},\tag{33}$$

then the bilinear form is positive-definite on V_h^{Γ} and so the trace finite element method (14) is well-posed. The solution u_h satisfies the a priori estimate,

$$\frac{c_0}{2}\|u_h\|^2_{L^2(\Gamma_h)}+\varepsilon\|\nabla_{\Gamma_h}u\|^2_{L^2(\Gamma_h)}\leq c_0^{-1}\|f\|^2_{L^2(\Gamma_h)}.\tag{34}$$

If $c_h=0$ and $\mathbf{w}_h=0$ on Γ_h (the Laplace–Beltrami problem), then one imposes the zero mean conditions for the solution and the right-hand side $\int_{\Gamma_h}f_h=\int_{\Gamma_h}u_h=0$ and proves the well-posedness result with the help of the Poincare inequality on Γ_h. For the mesh sufficiently fine, the Poincare constant is uniformly bounded independent of h, see Lemma 4.1 in [26].

To assess how restrictive the assumption in (33), we invoke the following estimates (Lemmas 3.5 and 3.6 in [23]) to bound the edge terms:

$$|\mathbf{P}(\mathbf{x})[\![\mathbf{m}_h]\!](\mathbf{x})|\lesssim h^2\quad\text{for }\mathbf{x}\in E,$$

and

$$\sum_{T\in\mathcal{F}_h}\int_{\partial T}v_h^2\,\mathrm{d}\mathbf{s}_h\lesssim h^{-1}\|v_h\|^2_{L^2(\Gamma_h)}+h\|\nabla_{\Gamma_h}v_h\|^2_{L^2(\Gamma_h)}\quad\text{for all } v_h\in V_h^{\Gamma}.$$

We remark that in [23] these estimates were proved for tetrahedra bulk subdivision, but all arguments carry over to cubic bulk meshes once we assume that the number of refinement level in octree is bounded. Since $\mathbf{P}\mathbf{w}^e=\mathbf{w}^e$, we get with $\mathbf{w}_h=\mathbf{w}^e$ on Γ_h:

$$\left|\sum_{T\in\mathcal{F}_h}\int_{\partial T}(\mathbf{w}_h\cdot[\![\mathbf{m}_h]\!])v_h^2\,\mathrm{d}\mathbf{r}\right|\lesssim h\|v_h\|^2_{L^2(\Gamma_h)}+h^3\|\nabla_{\Gamma_h}v_h\|^2_{L^2(\Gamma_h)}.$$

Therefore, we conclude that for sufficiently fine mesh, the bilinear form a_h is positive definite on V_h^{Γ} and so the discrete problem is well-posed under condition similar to the differential case: $c_h+\frac{1}{2}\mathrm{div}_{\Gamma_h}\mathbf{w}_h\geq c_0>0$ on Γ_h.

4.3. Consistency estimate

The consistency error of the finite element method (14) is due to geometric errors resulting from the approximation of Γ by Γ_h. To estimate these geometric errors, we need a few additional definitions and results, which can be found in, for example, [38]. For $\mathbf{x}\in\Gamma_h$ define $\tilde{\mathbf{P}}_h(\mathbf{x})=\mathbf{I}-\mathbf{n}_h(\mathbf{x})\mathbf{n}(\mathbf{x})^T/(\mathbf{n}_h(\mathbf{x})\cdot\mathbf{n}(\mathbf{x}))$. One can represent the surface gradient of $u\in H^1(\Gamma)$ in terms of $\nabla_{\Gamma_h}u^e$ as follows

$$\nabla_{\Gamma}u(\mathbf{p}(\mathbf{x}))=(\mathbf{I}-d(\mathbf{x})\mathbf{H}(\mathbf{x}))^{-1}\tilde{\mathbf{P}}_h(\mathbf{x})\nabla_{\Gamma_h}u^e(\mathbf{x})\quad\text{a.e. }\mathbf{x}\in\Gamma_h.$$

Due to (24), we get

$$\int_{\Gamma}\nabla_{\Gamma}u\nabla_{\Gamma}v\,\mathrm{d}\mathbf{s}=\int_{\Gamma_h}\mathbf{A}_h\nabla_{\Gamma_h}u^e\nabla_{\Gamma_h}v^e\,\mathrm{d}\mathbf{s}_h\quad\text{for all } v\in H^1(\Gamma),$$

with $\mathbf{A}_h(\mathbf{x})=\mu_h(\mathbf{x})\tilde{\mathbf{P}}_h^T(\mathbf{x})(\mathbf{I}-d(\mathbf{x})\mathbf{H}(\mathbf{x}))^{-2}\tilde{\mathbf{P}}_h(\mathbf{x})$. From $\mathbf{w}\cdot\mathbf{n}=0$ on Γ and $\mathbf{w}^e(\mathbf{x})=\mathbf{w}(\mathbf{p}(\mathbf{x}))$, $\mathbf{n}(\mathbf{x})=\mathbf{n}(\mathbf{p}(\mathbf{x}))$ it follows that $\mathbf{n}(\mathbf{x})\cdot\mathbf{w}^e(\mathbf{x})=0$ and thus $\mathbf{w}(\mathbf{p}(\mathbf{x}))=\tilde{\mathbf{P}}_h(\mathbf{x})\mathbf{w}^e(\mathbf{x})$ holds. Using this, we get the relation

$$\int_{\Gamma}(\mathbf{w}\cdot\nabla_{\Gamma}u)v\,\mathrm{d}\mathbf{s}=\int_{\Gamma_h}(\mathbf{B}_h\mathbf{w}^e\cdot\nabla_{\Gamma_h}u^e)v^e\,\mathrm{d}\mathbf{s}_h,$$

with $\mathbf{B}_h = \mu_h(\mathbf{x})\tilde{\mathbf{P}}_h^T (I - d\mathbf{H})^{-1}\tilde{\mathbf{P}}_h$. We shall use the lifting procedure $\Gamma_h \to \Gamma$ given by

$$v_h^l(\mathbf{p}(\mathbf{x})) := v_h(\mathbf{x}) \quad \text{for } \mathbf{x} \in \Gamma_h.$$

It is easy to see that $v_h^l \in H^1(\Gamma)$.

The following lemma estimates the consistency error of the finite element method (14).

Lemma 4.1. *Let $u \in H^2(\Gamma)$ be the solution of (5) and assume (31), then we have*

$$\sup_{v_h \in V_h^\Gamma} \frac{|f_h(v_h) - a_h(u^e, v_h)|}{\|v_h\|_{H^1(\Gamma_h)}} \lesssim h^2(\|u\|_{H^1(\Gamma)} + \|f\|_{L^2(\Gamma)}).$$

Proof. The residual is decomposed as

$$f_h(v_h) - a_h(u^e, v_h) = f_h(v_h) - f(v_h^l) + a(u, v_h^l) - a_h(u^e, v_h). \tag{35}$$

The following holds:

$$\begin{aligned} f(v_h^l) &= \int_\Gamma f v_h^l \,\mathrm{d}\mathbf{s} = \int_{\Gamma_h} \mu_h f^e v_h \,\mathrm{d}\mathbf{s}_h, \\ a(u, v_h^l) &= \varepsilon \int_\Gamma \nabla_\Gamma u \nabla_\Gamma v_h^l \,\mathrm{d}\mathbf{s} - \int_\Gamma (\mathbf{w} \cdot \nabla_\Gamma v_h^l) u \,\mathrm{d}\mathbf{s} + \int_\Gamma c\, u v_h^l \,\mathrm{d}\mathbf{s} \\ &= \varepsilon \int_{\Gamma_h} \mathbf{A}_h \nabla_{\Gamma_h} u^e \nabla_{\Gamma_h} v_h \,\mathrm{d}\mathbf{s}_h - \int_{\Gamma_h} (\mathbf{B}_h \mathbf{w}^e \cdot \nabla_{\Gamma_h} v_h) u^e \,\mathrm{d}\mathbf{s}_h + \int_{\Gamma_h} \mu_h c^e u^e v_h \,\mathrm{d}\mathbf{s}_h. \end{aligned}$$

Substituting these relations into (35) results in

$$\begin{aligned} f_h(v_h) - a_h(u^e, v_h) &= \int_{\Gamma_h} (1 - \mu_h) f^e v_h \,\mathrm{d}\mathbf{s}_h + \varepsilon \int_{\Gamma_h} (\mathbf{A}_h - \mathbf{P}_h) \nabla_{\Gamma_h} u^e \cdot \nabla_{\Gamma_h} v_h \,\mathrm{d}\mathbf{s}_h \\ &\quad - \int_{\Gamma_h} ((\mathbf{B}_h - \mathbf{P}_h)\mathbf{w}^e \cdot \nabla_{\Gamma_h} v_h) u^e \,\mathrm{d}\mathbf{s}_h + \int_{\Gamma_h} (\mu_h - 1) c^e u^e v_h \,\mathrm{d}\mathbf{s}_h =: I_1 + I_2 + I_3 + I_4. \end{aligned} \tag{36}$$

We estimate the I_i terms separately. Applying (25) we obtain

$$I_1 + I_4 \lesssim h^2 \|f^e\|_{L^2(\Gamma_h)} \|v_h\|_{L^2(\Gamma_h)}. \tag{37}$$

One can show, cf. (3.43) in [13], the bound

$$|\mathbf{P}_h - \mathbf{A}_h| = |\mathbf{P}_h(\mathbf{I} - \mathbf{A}_h)| \lesssim h^2.$$

Using this and (27) we obtain

$$I_2 \lesssim h^2 \|\nabla_{\Gamma_h} u^e\|_{L^2(\Gamma_h)} \|\nabla_{\Gamma_h} v_h\|_{L^2(\Gamma_h)} \lesssim h^2 \|u^e\|_{H^1(\Gamma)} \|v_h\|_{H^1(\Gamma_h)}. \tag{38}$$

Since $(\mathbf{I} - d\mathbf{H})^{-1} = \mathbf{I} + O(h^2)$, we also estimate

$$|\mathbf{B}_h - \mathbf{P}_h| \lesssim h^2 + |\mathbf{A}_h - \mathbf{P}_h| \lesssim h^2.$$

This yields

$$I_3 \lesssim h^2 \|\nabla_{\Gamma_h} v_h\|_{L^2(\Gamma_h)} \|u^e\|_{L^2(\Gamma_h)} \lesssim h^2 \|u\|_{H^1(\Gamma)} \|v_h\|_{H^1(\Gamma_h)}. \tag{39}$$

Combining the results (36)–(39) proves the lemma. □

4.4. Interpolation bounds

For a smooth function v defined on Γ consider its extension on Γ_h, v^e. In this subsection, we show that v^e can be approximated using the finite element trace space V_h^Γ with optimal order accuracy. First we need the following simple lemma.

Lemma 4.2. *Consider an arbitrary plane $\mathbb{P} \subset \mathbb{R}^3$ and any cubic cell $S \in \mathcal{T}_h$. It holds*

$$\|v\|^2_{L^2(S\cap\mathbb{P})} \lesssim h_S^{-1}\|v\|^2_{L^2(S)} + h_S\|\nabla v\|^2_{L^2(S)} \quad \forall\, v \in H^1(S). \tag{40}$$

Proof. The proof follows from the fact that any cubic cell is divided into a finite number of regular tetrahedra and further applying Lemma 4.2 from [39] on each of these tetrahedra. □

Now we are ready to prove the trace finite element interpolation bounds.

Theorem 4.1. *For arbitrary $v \in H^2(\Gamma)$ the following estimate holds with a constant c independent of h, v, and on how Γ_h intersects $\mathcal{T}_h$:*

$$\inf_{v_h\in V_h^\Gamma} \left(\|v^e - v_h\|_{L^2(\Gamma_h)} + h\|\nabla_{\Gamma_h}(v^e - v_h)\|_{L^2(\Gamma_h)}\right) \le ch^2\|v\|_{H^2(\Gamma)}. \tag{41}$$

Proof. Assume the maximum cell size h in $\mathcal{T}_h$ is attained at level k of the octree. Then the cells at the level k provide uniform cartesian subdivision which covers Ω. Denote this subdivision by $\mathcal{T}_h^k$ and the set of corresponding nodes by $\mathcal{N}_h^k$. Note that $v \in H^2(\Gamma)$ and $\Gamma \in C^2$ imply $v^e \in H^2(U_h)$ for the normal extension and we may define the nodal piecewise trilinear interpolant $I_h(v^e)$ such that $I_h(v^e)(\mathbf{x}) = v^e(\mathbf{x})$ for $\mathbf{x} \in \mathcal{N}_h^k \cap U_h$ and $I_h(v^e)(\mathbf{x}) = 0$ in other nodes. Since $\mathcal{T}_h^k$ does not contain hanging nodes, $I_h(v^e)$ is continuous and so it holds $I_h(v^e) \in V_h$.

Using the result in (40) and the interpolation properties of $I_h(v^e)$, we get for $v_h = I_h(v^e)|_{\Gamma_h}$:

$$\begin{aligned}
&\|v^e - v_h\|^2_{L^2(\Gamma_h)} + h^2\|\nabla_{\Gamma_h}(v^e - v_h)\|^2_{L^2(\Gamma_h)} = \sum_{T\in\mathcal{F}_h} \|v^e - v_h\|^2_{L^2(T)} + h^2\|\nabla_{\Gamma_h}(v^e - v_h)\|^2_{L^2(T)}\\
&\le \sum_{T\in\mathcal{F}_h} h_{S_T}^{-1}\|v^e - I_h(v^e)\|^2_{L^2(S_T)} + h^2h_{S_T}^{-1}\|\nabla(v^e - I_h(v^e))\|^2_{L^2(S_T)} + h^3\|\nabla^2(v^e - I_h(v^e))\|^2_{L^2(S_T)}\\
&\le C\,h^4h_{S_T}^{-1}\sum_{T\in\mathcal{F}_h}\|v^e\|^2_{H^2(S_T)}.
\end{aligned}$$

The assumption that the number of local refinement levels is bounded yields $hh_{S_T}^{-1} \le C$. Hence, it holds

$$\|v^e - v_h\|^2_{L^2(\Gamma_h)} + h^2\|\nabla_{\Gamma_h}(v^e - v_h)\|^2_{L^2(\Gamma_h)} \le h^3\|v^e\|^2_{H^2(U_h)}.$$

It remains to apply (30). □

4.5. Error estimates

Now we combine the results derived in the previous sections to prove the first error estimate.

Theorem 4.2. *Assume u is the solution of (5) and let u_h be the discrete solution of the trace finite element method (14). Then the following estimate holds:*

$$\|u^e - u_h\|_{H^1(\Gamma_h)} \lesssim h\|f\|_{L^2(\Gamma)}. \tag{42}$$

Proof. Consider an interpolant $(I_hu^e) \in V_h$ from Theorem 4.1. The triangle inequality yields

$$\|u^e - u_h\|_{H^1(\Gamma_h)} \le \|u^e - (I_hu^e)|_{\Gamma_h}\|_{H^1(\Gamma_h)} + \|(I_hu^e)|_{\Gamma_h} - u_h\|_{H^1(\Gamma_h)}. \tag{43}$$

The second term in the upper bound can be estimated using coercivity, continuity of the finite element bilinear form, interpolation properties from Theorem 4.1, and the consistency estimate in Lemma 4.1:

$$\begin{aligned}
&\|(I_hu^e)|_{\Gamma_h} - u_h\|^2_{H^1(\Gamma_h)} \lesssim a_h((I_hu^e)|_{\Gamma_h} - u_h, (I_hu^e)|_{\Gamma_h} - u_h)\\
&= a_h((I_hu^e)|_{\Gamma_h} - u^e, (I_hu^e)|_{\Gamma_h} - u_h) + a_h(u^e - u_h, (I_hu^e)|_{\Gamma_h} - u_h)\\
&\lesssim h\|u\|_{H^2(\Gamma)}\|(I_hu^e)|_{\Gamma_h} - u_h\|_{H^1(\Gamma_h)} + |a_h(u^e, (I_hu^e)|_{\Gamma_h} - u_h) - f_h((I_hu^e)|_{\Gamma_h} - u_h)|\\
&\lesssim h\big(\|u\|_{H^2(\Gamma)} + \|f\|_{L^2(\Gamma)}\big)\|(I_hu^e)|_{\Gamma_h} - u_h\|_{H^1(\Gamma_h)}.
\end{aligned}$$

This results in

$$\|(I_h u^e)|_{\Gamma_h} - u_h\|_{H^1(\Gamma_h)} \lesssim h(\|u\|_{H^2(\Gamma)} + \|f\|_{L^2(\Gamma)}). \tag{44}$$

The error estimate (42) follows from (43), (44), (41), and $\|u\|_{H^2(\Gamma)} \lesssim \|f\|_{L^2(\Gamma)}$. □

We now apply a duality argument to obtain an $L^2(\Gamma_h)$ error bound.

Theorem 4.3. *Additionally assume that (9) and (33) hold with* $\mathbf{w}$ *replaced by* $-\mathbf{w}$. *With the same* u, u_h *as in Theorem 4.2, the following error bound holds*

$$\|u^e - u_h\|_{L^2(\Gamma_h)} \lesssim h^2 \|f\|_{L^2(\Gamma)}. \tag{45}$$

Proof. Denote $e_h := (u^e - u_h)|_{\Gamma_h}$ and let e_h^l be the lift of e_h on Γ. Consider the problem: Find $w \in H^1(\Gamma)$, such that

$$a(v, w) = \int_\Gamma e_h^l v \, \mathrm{d}\mathbf{s} \quad \text{for all } v \in H^1(\Gamma). \tag{46}$$

The problem is well-posed and the solution w satisfies $w \in H^2(\Gamma)$ and $\|w\|_{H^2(\Gamma)} \lesssim \|e_h^l\|_{L^2(\Gamma)}$. Furthermore, $\|w^e\|_{H^1(\Gamma_h)} \lesssim \|w\|_{H^1(\Gamma)} \lesssim \|e_h^l\|_{L^2(\Gamma)}$. Due to (46) we have, for any $\psi_h \in V_h^\Gamma$,

$$\begin{aligned}\|e_h^l\|^2_{L^2(\Gamma)} &= a(e_h^l, w) = a(e_h^l, w) - a_h(e_h, w^e) + a_h(e_h, w^e - \psi_h) + a_h(e_h, \psi_h) \\ &= \left[a(e_h^l, w) - a_h(e_h, w^e)\right] + a_h(e_h, w^e - \psi_h) + \left[a_h(u^e, \psi_h) - f_h(\psi_h)\right]. \end{aligned} \tag{47}$$

We let $\psi_h = (I_h u^e) \in V_h$, interpolant given by Theorem 4.1. The terms on the right hand side of (47) are treated separately. The bound for the third one follows from Lemma 4.1:

$$a_h(u^e, \psi_h) - f_h(\psi_h) \lesssim h^2(\|u\|_{H^1(\Gamma)} + \|f\|_{L^2(\Gamma)})\|\psi_h\|_{H^1(\Gamma_h)} \lesssim h^2(\|u\|_{H^1(\Gamma)} + \|f\|_{L^2(\Gamma)})\|u^e\|_{H^2(\Gamma)}. \tag{48}$$

The bound for the second term follows from the continuity of the bilinear form, interpolation properties in Theorem 4.1 and the error bound in Theorem 4.2:

$$a_h(e_h, w^e - \psi_h) \lesssim \|e_h\|_{H^1(\Gamma_h)}\|w^e - \psi_h\|_{H^1(\Gamma_h)} \lesssim h^2\|f\|_{L^2(\Gamma)}\|w^e\|_{H^2(\Gamma)}. \tag{49}$$

For the first term we get the expression similar to (36):

$$\begin{aligned} a(e_h^l, w) - a_h(e_h, w^e) = \varepsilon &\int_{\Gamma_h} (\mathbf{A}_h - \mathbf{P}_h)\nabla_{\Gamma_h} w^e \cdot \nabla_{\Gamma_h} e_h \, \mathrm{d}\mathbf{s}_h \\ &- \int_{\Gamma_h} ((\mathbf{B}_h - \mathbf{P}_h)\mathbf{w}^e \cdot \nabla_{\Gamma_h} w^e) e_h \, \mathrm{d}\mathbf{s}_h + \int_{\Gamma_h} (\mu_h - 1) c^e w^e e_h \, \mathrm{d}\mathbf{s}_h. \end{aligned}$$

Hence, repeating the same argument as in the proof of Lemma 4.1, we get

$$a(e_h^l, w) - a_h(e_h, w^e) \lesssim h^2\|e_h\|_{H^1(\Gamma_h)}\|w^e\|_{H^1(\Gamma)}.$$

Further, employing the error bound from Theorem 4.2, we have

$$a(e_h^l, w) - a_h(e_h, w^e) \lesssim h^3\|f\|_{L^2(\Gamma)}\|w^e\|_{H^1(\Gamma)}. \tag{50}$$

Combining (47)–(50) with the regularity result for the solution of the dual problem (46) completes the proof. □

4.6. A posteriori estimate and error indicator

In this section, we deduce an a posteriori error estimate for the trace FEM. Based on this estimate we define a residual type error indicator, which we use for a mesh adaptation purpose. We will treat only the formulation with surface gradient (14) and assume that the Peclet number is sufficiently small and hence no additional stabilization is needed.

Consider the surface finite element error $e_h = u^e - u_h$ on Γ_h. We prove an a posteriori bound for the lift of e_h on Γ, i.e. $e_h^l = u - u_h^l$ on Γ. Thanks to (9) the functional $\|[v]\| := (\varepsilon\|\nabla_\Gamma v\|^2_{L_2(\Gamma)} + \|(c + \frac{1}{2}\mathrm{div}_\Gamma \mathbf{w})\, v\|^2_{L_2(\Gamma)})^{\frac{1}{2}}$ defines a norm on V such that

$$\|[e_h^l]\| \le \sup_{\psi:\ \|[\psi]\|=1} \int_\Gamma a(e_h^l, \psi)\, \mathrm{d}\mathbf{s}. \tag{51}$$

Now we let $\psi \in V$ with $\|[\psi]\| = 1$. For arbitrary $\psi_h \in V_h$, observe the identities

$$\begin{aligned}
a(e_h^l, \psi) &= \int_\Gamma f\psi\, d\mathbf{s} - a(u_h^l, \psi) \\
&= \int_{\Gamma_h} f^e \mu_h (\psi^e - \psi_h)\, d\mathbf{s}_h + \int_{\Gamma_h} (f^e\mu_h - f^e)\psi_h\, d\mathbf{s}_h + a_h(u_h, \psi_h) - a(u_h^l, \psi) \\
&= \int_{\Gamma_h} f^e \mu_h (\psi^e - \psi_h)\, d\mathbf{s}_h + \int_{\Gamma_h} f^e(\mu_h - 1)\psi_h\, d\mathbf{s}_h + a_h(u_h, \psi_h - \psi^e) \\
&\quad - \left[\varepsilon \int_{\Gamma_h} (\mathbf{A}_h - \mathbf{P}_h)\nabla_{\Gamma_h} u_h \cdot \nabla_{\Gamma_h}\psi^e\, \mathrm{d}\mathbf{s}_h - \frac{1}{2}\int_{\Gamma_h} ((\mathbf{B}_h - \mathbf{P}_h)\mathbf{w}^e \cdot \nabla_{\Gamma_h}\psi^e) u_h\, \mathrm{d}\mathbf{s}_h \right. \\
&\quad \left. + \int_{\Gamma_h} (\mu_h - 1) c^e u_h \psi^e\, \mathrm{d}\mathbf{s}_h \right].
\end{aligned} \tag{52}$$

We apply elementwise integration by parts to the third term on the right hand side of (52):

$$\begin{aligned}
a_h(u_h, \psi_h - \psi^e) &= \int_{\Gamma_h} (\varepsilon \Delta_{\Gamma_h} u_h - (c_h + \mathrm{div}_{\Gamma_h}\mathbf{w}_h)u_h - \mathbf{w}_h \cdot \nabla_{\Gamma_h} u_h)(\psi^e - \psi_h)\, \mathrm{d}\mathbf{s}_h \\
&\quad - \frac{1}{2}\sum_{T\in\mathcal{F}_h} \int_{\partial T} \varepsilon [\![\nabla_{\Gamma_h} u_h]\!](\psi^e - \psi_h)\, \mathrm{d}\mathbf{r} + \frac{1}{2}\sum_{T\in\mathcal{F}_h}\int_{\partial T} (\mathbf{w}_h \cdot [\![\mathbf{m}_h]\!]) u_h (\psi^e - \psi_h)\, \mathrm{d}\mathbf{r},
\end{aligned} \tag{53}$$

where $[\![\nabla_{\Gamma_h} u_h]\!]$ denotes the jump in the normal derivative across an edge of T. Substituting (53) into (52) and applying the Cauchy inequality elementwise over $\mathcal{F}_h$, we get

$$\begin{aligned}
a(e_h^l, \psi) \lesssim &\left(\sum_{T\in\mathcal{F}_h} |1-\mu_h|^2_{L^\infty(T)} \left(\|f^e\|^2_{L^2(T)} + \|u_h\|^2_{L^2(T)} \right) + \|\mathbf{A}_h - \mathbf{P}_h\|^2_{L^\infty(T)} \|\nabla_{\Gamma_h} u_h\|^2_{L^2(T)} \right. \\
&\left. + \|\mathbf{B}_h - \mathbf{P}_h\|^2_{L^\infty(T)} \|u_h\|^2_{L^2(T)} \right)^{\frac{1}{2}} \|\psi^e\|_{H^1(\Gamma_h)} + \left(\sum_{T\in\mathcal{F}_h} \left[\eta_R(T)^2 + \eta_E(T)^2 \right] \right)^{\frac{1}{2}} \\
&\times \left(\sum_{T\in\mathcal{F}_h} \left[h_{S_T}^{-2} \|\psi^e - \psi_h\|^2_{L^2(T)} + \sum_{e\in\partial T} h_{S_T}^{-1} \|\psi^e - \psi_h\|^2_{L^2(e)} \right] \right)^{\frac{1}{2}},
\end{aligned} \tag{54}$$

with

$$\begin{aligned}
\eta_R(T)^2 &= h_{S_T}^2 \| f_h + \varepsilon \Delta_{\Gamma_h} u_h - (c_h + \mathrm{div}_{\Gamma_h}\mathbf{w}_h)u_h - \mathbf{w}_h \cdot \nabla_{\Gamma_h} u_h \|^2_{L^2(T)} \\
\eta_E(T)^2 &= \sum_{e\in\partial T} h_{S_T} \left(\|[\![\varepsilon \nabla_{\Gamma_h} u_h]\!]\|^2_{L^2(e)} + \|\mathbf{w}_h \cdot [\![\mathbf{m}_h]\!]\|^2_{L^2(e)} \right).
\end{aligned}$$

Combining (51) and (54) leads to an a posteriori error estimate, where ψ-dependent terms on the right hand side should be handled further. Due to (24) and (27) we have

$$\|\psi^e\|_{H^1(\Gamma_h)} \lesssim \|\psi\|_{H^1(\Gamma)}. \tag{55}$$

For every $e \in \partial T$ denote by $T_e \subset S_T$ a plane segment of the regular shape such that $\mathrm{diam}(T_e) \simeq h_{S_T}$. We apply the result in (40) and its two-dimensional analog to estimate

$$
\begin{aligned}
&h_{S_T}^{-2}\|\psi^e-\psi_h\|^2_{L^2(T)}+\sum_{e\in\partial T} h_{S_T}^{-1}\|\psi^e-\psi_h\|^2_{L^2(e)}\\
&\quad\lesssim h_{S_T}^{-3}\|\psi^e-\psi_h\|^2_{L^2(S_T)}+h_{S_T}^{-1}\|\nabla(\psi^e-\psi_h)\|^2_{L^2(S_T)}\\
&\qquad+\sum_{e\in\partial T}\left(h_{S_T}^{-2}\|\psi^e-\psi_h\|^2_{L^2(T_e)}+\|\nabla(\psi^e-\psi_h)\|^2_{L^2(T_e)}\right)\\
&\quad\lesssim h_{S_T}^{-3}\|\psi^e-\psi_h\|^2_{L^2(S_T)}+h_{S_T}^{-1}\|\nabla(\psi^e-\psi_h)\|^2_{L^2(S_T)}+\sum_{e\in\partial T}\left(\|\nabla\psi^e\|^2_{L^2(T_e)}+\|\nabla\psi_h\|^2_{L^2(T_e)}\right)\\
&\quad\lesssim h_{S_T}^{-3}\|\psi^e-\psi_h\|^2_{L^2(S_T)}+h_{S_T}^{-1}\|\nabla(\psi^e-\psi_h)\|^2_{L^2(S_T)}+\left(\|\nabla_\Gamma\psi\|^2_{L^2(\mathbf{p}(S_T))}+h_{S_T}^{-1}\|\nabla\psi_h\|^2_{L^2(S_T)}\right).
\end{aligned}
\tag{56}
$$

In this paper we consider only graded octree meshes. In terms of [40], these are 1-irregular meshes and hence for $\psi^e\in H^1(\Omega)$ (assuming arbitrary smooth extension of ψ^e from U_h to Ω) one can consider a Scott–Zhang type interpolant $\psi_h\in V_h$ such that

$$
h_S^{-1}\|\psi^e-\psi_h\|_{L^2(S)}+\|\nabla\psi_h\|_{L^2(S)}\lesssim\|\psi^e\|_{H^1(\omega(S))}\quad\forall\, S\in\Omega_h,
\tag{57}
$$

where $\omega(S)$ is defined as follows: Let $\tilde\omega(S)$ consist of S and of all cubic cells touching S, then $\omega(S)$ is a patch of cells defined as the union of $\tilde\omega(S)$ and of all cubic cells touching $\tilde\omega(S)$. We assume $\tilde c$ in (20) to be sufficiently large and h sufficiently small that $\omega(S)\subset U_h$ for all $S\in\Omega_h$. Applying (57) in (56) yields

$$
\begin{aligned}
&\sum_{T\in\mathcal{F}_h}\left[h_{S_T}^{-2}\|\psi^e-\psi_h\|^2_{L^2(T)}+\sum_{e\in\partial T}h_{S_T}^{-1}\|\psi^e-\psi_h\|^2_{L^2(e)}\right]\lesssim\sum_{T\in\mathcal{F}_h}\left(h_{S_T}^{-1}\|\psi^e\|^2_{H^1(\omega(S_T))}+\|\nabla_\Gamma\psi\|^2_{L^2(\mathbf{p}(S_T))}\right)\\
&\quad\lesssim\sum_{T\in\mathcal{F}_h}\|\psi\|^2_{H^1(\mathbf{p}(\omega(S_T)))}\simeq\sum_{S\in\Omega_h}\|\psi\|^2_{H^1(\mathbf{p}(\omega(S)))}.
\end{aligned}
\tag{58}
$$

In the last inequality we used the fact that for the graded octree mesh $\operatorname{diam}(\omega(S_T))\simeq h_{S_T}$. For any two patches $\omega(S_1)$ and $\omega(S_2)$, $S_1,S_2\in\Omega_h$, the number of cubic cells in $\omega(S_1)\cap\omega(S_2)$ is bounded by a constant independent of h and the number of refinement levels. However, for the projections on Γ the intersection $\mathbf{p}(\omega(S_1))\cap\mathbf{p}(\omega(S_2))$ may be nonempty, even if two patches do not overlap. Thus $\mathbf{x}\in\Gamma$ may belong to the projections of patches for several cells in Ω_h, but the number of such patches may not grow faster than $O(K)$ uniformly over Γ, where K is the number of the levels in the octree. Therefore it holds

$$
\sum_{T\in\mathcal{F}_h}\|\psi\|^2_{H^1(\mathbf{p}(\omega(S_T)))}\lesssim K\|\psi\|^2_{H^1(\Gamma)}.
\tag{59}
$$

We assumed that the number of levels is uniformly bounded for the family of meshes and so $K=O(1)$, while in general case it holds $K\lesssim|\ln h_{\min}|$. Using (56)–(59), we prove the existence of $\psi_h\in V_h$ such that

$$
\sum_{T\in\mathcal{F}_h}\left[h_{S_T}^{-2}\|\psi^e-\psi_h\|^2_{L^2(T)}+\sum_{e\in\partial T}h_{S_T}^{-1}\|\psi^e-\psi_h\|^2_{L^2(e)}\right]\lesssim\|\psi\|^2_{H^1(\Gamma)}.
\tag{60}
$$

Combining (51) and (55), (60) gives the following *a posteriori* error estimate

$$
\begin{aligned}
\|[e_h^l]\|\lesssim\Bigg(&\sum_{T\in\mathcal{F}_h}|1-\mu_h|^2_{L^\infty(T)}\left(\|f^e\|^2_{L^2(T)}+\|u_h\|^2_{L^2(T)}\right)+\|\mathbf{A}_h-\mathbf{P}_h\|^2_{L^\infty(T)}\|\nabla_{\Gamma_h}u_h\|^2_{L^2(T)}\\
&+\|\mathbf{B}_h-\mathbf{P}_h\|^2_{L^\infty(T)}\|u_h\|^2_{L^2(T)}\Bigg)^{\frac12}+\left(\sum_{T\in\mathcal{F}_h}\left[\eta_R(T)^2+\eta_E(T)^2\right]\right)^{\frac12}.
\end{aligned}
\tag{61}
$$

Finally, if we assume that local grid refinement leads to better local surface reconstruction, i.e. (22) and (23) can be formulated locally, then the first term on the right-hand side of (61) is of higher order. We may assume $|1-\mu_h|^2_{L^\infty(T)}+\|\mathbf{A}_h-\mathbf{P}_h\|^2_{L^\infty(T)}+\|\mathbf{B}_h-\mathbf{P}_h\|^2_{L^\infty(T)}\lesssim h_{S_T}^4\|\mathbf{H}\|^2_{L^\infty(\mathbf{p}(T))}$. This suggests introducing also the geometric

error indicator

$$\eta_G(T)^2 := h_{S_T}^4 \|\mathbf{H}_h\|^2_{L^\infty(T)} \left(\|f^e\|^2_{L^2(T)} + \|u_h\|^2_{H^1(T)} \right),$$

where $\mathbf{H}_h$ is a Hessian reconstruction on Γ_h.

Thus, for the purpose of local mesh adaptation we use the following error indicator:

$$\eta(T) := (\alpha_r \eta_R(T)^2 + \alpha_e \eta_E(T)^2 + \alpha_g \eta_G(T)^2)^{\frac{1}{2}} \tag{62}$$

with some parameters $\alpha_r, \alpha_e, \alpha_g \geq 0$. We set α_g equal to 0 or 1 depending on whether we wish to account (explicitly) for geometric errors or not. For regular elliptic problems we set $\alpha_r = \alpha_e = 1$, while for transport dominated problems more weight is put on the edge error indicator (see next section). We also note that the second edge term in the definition of $\eta_E(T)^2$ is of higher order. Our numerical experience suggests that it can be excluded without any notable change in the performance of an adaptive method.

Results of experiments in the next section show that the trace FE adaptive method based on $\eta(T)$ and standard "maximum" marking strategy leads to optimal convergence of the error in H^1 and L^2 norms.

5. Numerical examples

5.1. Smooth solutions on a sphere and a torus

Example 1. As a first test problem we consider the Laplace–Beltrami type equation on the unit sphere:

$$-\Delta_\Gamma u + u = f \quad \text{on } \Gamma,$$

with $\Gamma = \{\mathbf{x} \in \mathbb{R}^3 \mid \|\mathbf{x}\|_2 = 1\}$ and $\Omega = (-2, 2)^3$. The source term f is taken such that the solution is given by

$$u(\mathbf{x}) = \frac{a}{\|\mathbf{x}\|^3} \left(3x_1^2 x_2 - x_2^3 \right), \quad \mathbf{x} = (x_1, x_2, x_3) \in \Omega,$$

with $a = 12$. Using the representation of u in spherical coordinates one can verify that u is an eigenfunction of $-\Delta_\Gamma$: $u(r, \phi, \theta) = a \sin(3\phi) \sin^3\theta$, $-\Delta_\Gamma u + u = 13u =: f(r, \phi, \theta)$. Both u and f are constant along normals at Γ.

Example 2. In the second example, we consider a torus instead of the unit sphere and the same equation: $\Gamma \subset \Omega = (-2, 2)^3$, with $\Gamma = \{\mathbf{x} \in \Omega \mid r^2 = x_3^2 + (\sqrt{x_1^2 + x_2^2} - R)^2\}$. We take $R = 1$ and $r = 0.6$. In the coordinate system (ρ, ϕ, θ), with

$$\mathbf{x} = R \begin{pmatrix} \cos\phi \\ \sin\phi \\ 0 \end{pmatrix} + \rho \begin{pmatrix} \cos\phi\cos\theta \\ \sin\phi\cos\theta \\ \sin\theta \end{pmatrix},$$

the ρ-direction is normal to Γ, $\frac{\partial \mathbf{x}}{\partial \rho} \perp \Gamma$ for $\mathbf{x} \in \Gamma$. Thus, the following solution u and corresponding right-hand side f are constant in the normal direction:

$$\begin{aligned} u(\mathbf{x}) &= \sin(3\phi)\cos(3\theta + \phi), \\ f(\mathbf{x}) &= r^{-2}(9\sin(3\phi)\cos(3\theta + \phi)) - (R + r\cos(\theta))^{-2}(-10\sin(3\phi)\cos(3\theta + \phi) - 6\cos(3\phi)\sin(3\theta + \phi)) \\ &\quad - r(R + r\cos(\theta))^{-1}(3\sin(\theta)\sin(3\phi)\sin(3\theta + \phi)) + u(\mathbf{x}). \end{aligned} \tag{63}$$

We compute numerical solutions to Examples 1 and 2 using the trace FE methods (14) and (16) on a sequence of octree bulk grids. The initial grid was uniform with $h = \frac{1}{4}$. Further the grid was gradely refined towards the surfaces. All linear algebra systems in this and further experiments were solved with the help of PETSc library: We computed LU factorizations of diagonally scaled stiffness matrices. Finite element errors and convergence rates are shown in Table 1. Both variants demonstrate second order convergence in L^2 surface norm and close to second order in L^∞ surface norm. Computed solutions and final meshes are visualized in Fig. 3.

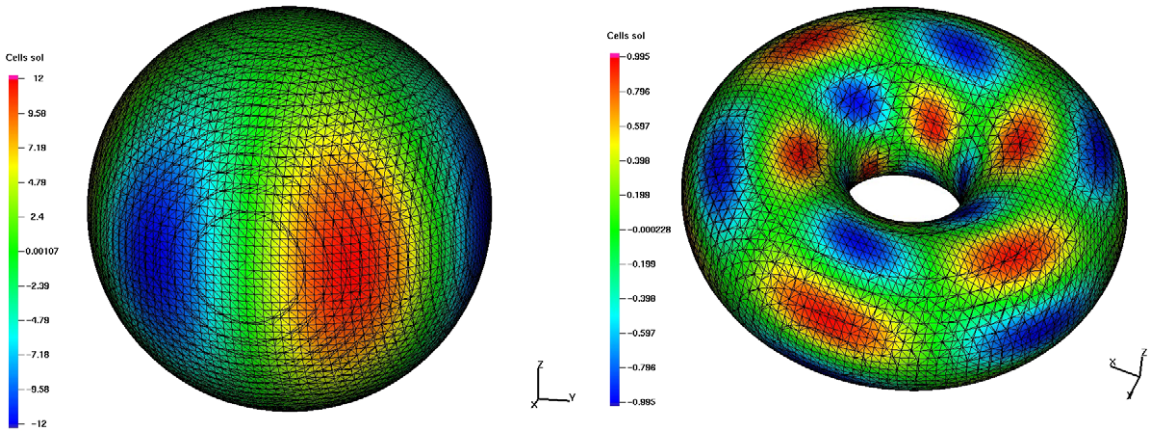

Fig. 3. The numerical solutions and surface meshes from Examples 1 and 2.

Table 1
Surface gradient and full gradient trace FEM convergence for uniform mesh refinement and smooth solutions.

	#d.o.f.	Surface gradient variant (14)				Full gradient variant (16)			
		L^2-norm	Rate	L^∞-norm	Rate	L^2-norm	Rate	L^∞-norm	Rate
Sphere	292	2.672e−1		6.631e−1		6.041e−1		1.257e−0	
	1,398	5.813e−2	2.20	1.462e−1	2.18	1.418e−1	2.09	3.959e−1	1.67
	5,960	1.366e−2	2.09	4.032e−2	1.86	3.566e−2	1.99	1.031e−1	1.94
	24,730	3.364e−3	2.02	1.138e−2	1.86	8.891e−3	2.00	2.582e−2	2.00
Torus	297	2.415e−1		7.898e−1		3.199e−1		8.861e−1	
	1,289	5.047e−2	2.26	2.123e−1	1.90	8.406e−2	1.93	4.437e−1	0.98
	5,001	1.049e−2	2.27	5.400e−2	1.98	1.956e−2	2.10	8.562e−2	2.37
	20,073	2.367e−3	2.15	1.341e−2	2.01	4.979e−3	1.97	2.184e−2	1.97

5.2. *Smooth solutions on more complicated geometries*

To demonstrate the flexibility of the method with respect to the shape of Γ, we consider the Laplace–Beltrami equation on two geometrically more complicated surfaces. Both examples of surfaces can be found in [12].

Example 3. The first surface is given by the zero of the level set function

$$\phi(\mathbf{x}) = \frac{1}{4}x_1^2 + x_2^2 + \frac{4x_3^2}{(1+\frac{1}{2}\sin(\pi x_1))^2} - 1.$$

The exact solution to (5) with $\mathbf{w} = 0$, $\varepsilon = 1$, $c = 1$, is taken very regular, $u = x_1x_2$ on Γ. The surface is illustrated in Fig. 4. The normal vector on Γ is $\mathbf{n} = \nabla\phi/|\nabla\phi| =: (n_1, n_2, n_3)^T$ and $\mathbf{H}$ can be computed from $\mathbf{H} = \nabla_\Gamma \mathbf{n}$. The entries of $\mathbf{H}$ are given by

$$\mathbf{H}_{im} = \frac{1}{|\nabla\phi|}\left(\phi_{x_ix_m} - \frac{\phi_{x_i}\left(\sum_{k=1}^{3}\phi_{x_k}\phi_{x_kx_m}\right) + \phi_{x_m}\left(\sum_{j=1}^{3}\phi_{x_j}\phi_{x_ix_j}\right)}{|\nabla\phi|^2} + \frac{\phi_{x_i}\phi_{x_m}\left(\sum_{j=1}^{3}\sum_{k=1}^{3}\phi_{x_k}\phi_{x_kx_j}\right)}{|\nabla\phi|^4}\right)$$

for $i, m = 1, 2, 3$. The right-hand side is then given by

$$f(\mathbf{x}) = x_1x_2 + 2n_1(\mathbf{x})n_2(\mathbf{x}) + \mathrm{tr}(\mathbf{H}(\mathbf{x}))(x_1n_2(\mathbf{x}) + x_2n_1(\mathbf{x})), \quad \mathbf{x} \in \Gamma.$$

Fig. 4 shows the numerical solution and plots it over the trace mesh, which results after 9 steps of adaptation, starting with the uniform cubic mesh with $h = 1/4$. Here and in any further adaptive mesh refinement we employ

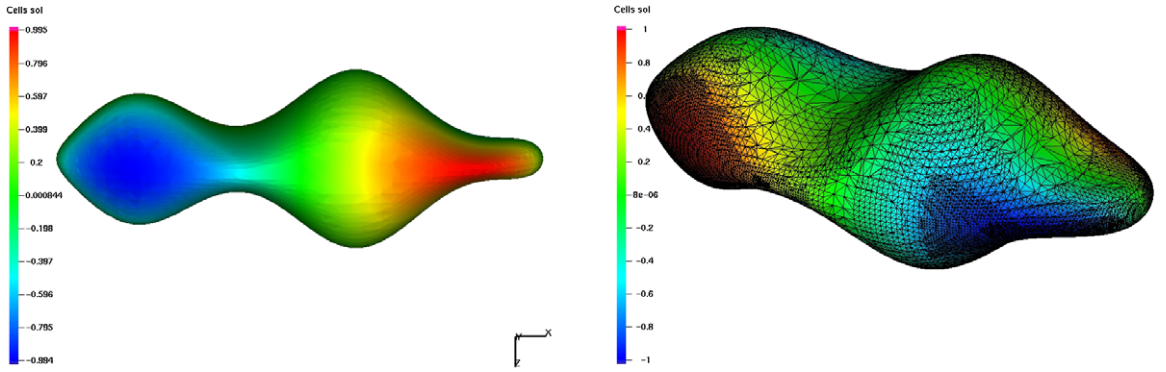

Fig. 4. Illustration of the surface and solution from Example 3. The right figure shows also triangulation after 7 steps of adaptation based on the error indicator.

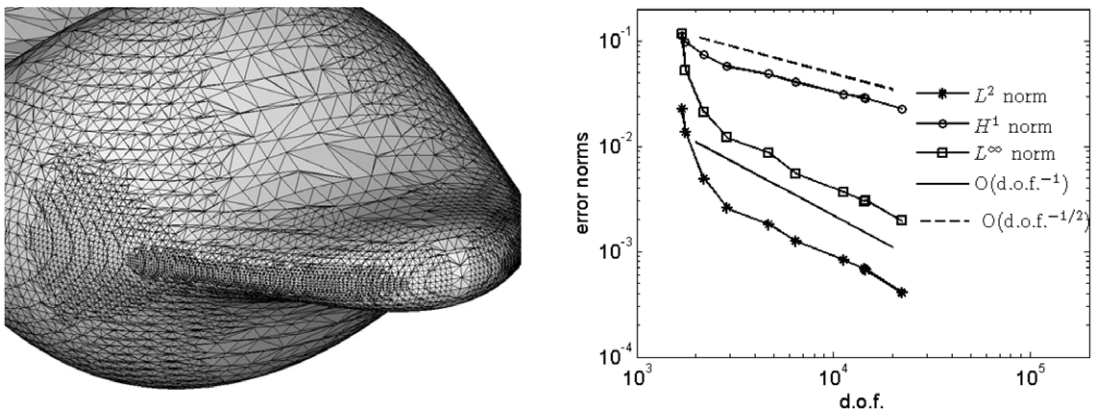

Fig. 5. Left: Adaptive trace FEM convergence in Example 3. Right: The zoom of the trace surface mesh in Example 3. The adaptation was based on the residual indicator accounting for geometric errors.

a "maximum" marking strategy in which all volume cubes S from ω_h with $\eta(S) > \frac{1}{2}\max_{S\in\omega_h}\eta(S)$ are marked for further refinement. Note that some adjunct cubes also may need refinement if one wishes to keep the octree balanced. Fig. 5 (right) displays the finite element error reduction if the mesh adaptation process is based on the error indicator (62). The results demonstrate optimal convergence order of the adaptive trace FEM with respect to the total number of degrees of freedom in L^2, H^1 and L^∞ surface norms. The results are shown for the surface gradient variant of the method (14). Here and further "number of d.o.f." means only the number of active degrees of freedom, which is equal to the dimension of the resulting system of linear algebraic equations. We set $\alpha_g = 1$ in the error indicator to account for geometric errors. The left plot in Fig. 5 zooms the trace surface mesh. From this plot we see that the mesh refinement generally happens in regions with higher surface curvatures.

Example 4. This is another example of a more complicated domain, which is homeomorphic to the sphere with 6 handles, see Fig. 6. The surface is given implicitly as the zero level set of

$$\phi = (x_1^2 + x_2^2 - 4)^2 + (x_2^2 - 1)^2 + (x_2^2 + x_3^2 - 4)^2 + (x_1^2 - 1)^2 + (x_1^2 + x_3^2 - 4)^2 + (x_3^2 - 1)^2 - 13.$$

We solve the Laplace–Beltrami equation with right-hand side $f = 100\sum_{j=1}^{4}\exp(-|\mathbf{x} - \mathbf{x}^j|^2)$, with

$$\mathbf{x}^1 = (-1, 1, 2.04), \qquad \mathbf{x}^2 = (1, 2.04, 1), \qquad \mathbf{x}^3 = (2.04, 0, 1), \qquad \mathbf{x}^4 = (-0.-1, -2.04).$$

The points are close to the surface and the right-hand side is varying rapidly in vicinities of these 4 points, and hence the same is expected from the solution. The solution and the grid resulted after 12 steps of refinement are visualized in Fig. 6. The refinement was based on the error indicator (62) with $\alpha_g = 1$.

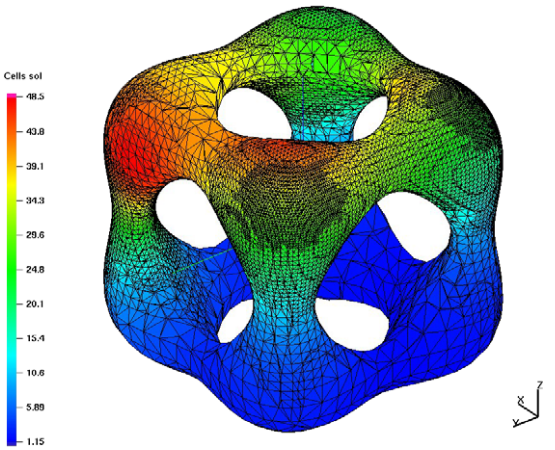

Fig. 6. The surface, numerical solution and adaptive mesh from Example 4.

5.3. Laplace–Beltrami problem with point singularity

Example 5. For the next test problem we consider the Laplace–Beltrami equation on the unit sphere. The solution and the source term in spherical coordinates are given by

$$u = \sin^{\lambda}\theta\sin\phi, \qquad f = (1+\lambda^2+\lambda)\sin^{\lambda}\theta\sin\phi + (1-\lambda^2)\sin^{\lambda-2}\theta\sin\phi. \tag{64}$$

One verifies

$$\nabla_{\Gamma} u = \sin^{\lambda-1}\theta\left(\frac{1}{2}\sin 2\phi\,(\lambda\cos^2\theta - 1),\ \sin^2\phi(\lambda\cos^2\theta - 1) + 1,\ -\frac{1}{2}\lambda\sin 2\theta\sin\phi\right)^T.$$

For $\lambda < 1$ the solution u is singular at the north and south poles of the sphere so that $u \in H^1(\Gamma)$, but $u \notin H^2(\Gamma)$. Following [38] we set $\lambda = 0.6$ to model the point singularity and contrast it to the regular problem with $\lambda = 1$.

Results produced by the adaptive algorithm are shown in Fig. 7, where they are compared to the results for uniform grid refinement. As expected, the regular refinement leads to a suboptimal convergence for the singular case of $\lambda = 0.6$. Adaptive refinement driven by the error indicator (62) leads to optimal convergence rates in L^2 and H^1 surface norms. Note that reliability of the error indicator for H^1 error norm was proved in [25] for tetrahedral meshes. A posteriori error analysis in other norms remains an open question.

The left column in Fig. 7 displays error decrease for the surface gradient formulation (14), while the right column of plots displays error decrease for the full gradient formulation (16). Similar to regular problems and regular refinement in Examples 1 and 2, the adaptive algorithm shows close performance for both formulations producing slightly more accurate results for the surface gradient formulation (14).

Fig. 8 (left) displays a cutaway view which includes both the adaptively refined bulk and surface meshes. The meshes are shown after the 12 refinement steps. The middle picture in Fig. 8 shows the surface mesh superimposed on numerical solution. The coarsest mesh is in the regions with the smallest solution gradient. Fig. 8 (right) displays the surface mesh near the north pole magnified 20 times. This local mesh appears more structured, since the surface is locally close to a plane which cuts through a regular bulk mesh.

5.4. Convection–diffusion problem with an internal layer

We now perform several tests for the advection–diffusion problem as in (5), with nonzero advection field $\mathbf{w}$. As usual, the properties of the problem essentially depend on the value of the dimensionless Peclet number. The Peclet number can be defined similar to volumetric case as $Pe = \frac{LW}{2\varepsilon}$, where L is a characteristic problem scale (say, the diameter of a closed surface Γ) and W is a characteristic advection velocity. For low values of the Peclet numbers, the problem is close to the Laplace–Beltrami equation, while for higher Peclet numbers, the problem may demonstrate behavior typical to singular-perturbed equations, e.g., its solution may exhibit internal layers. The example considered

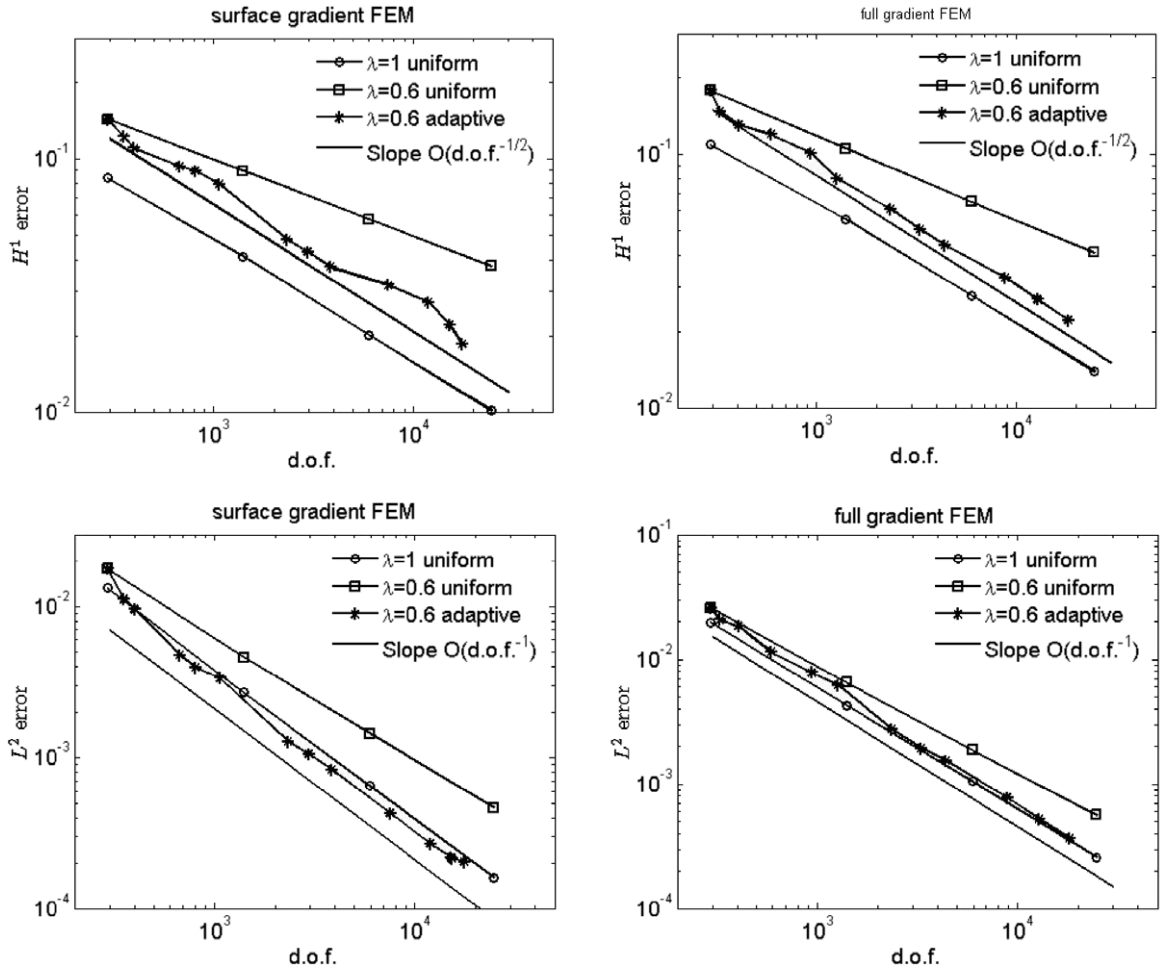

Fig. 7. Decrease of the error in $H^1(\Gamma_h)$-norm (upper plots), $L^2(\Gamma_h)$-norm (bottom plots) for the adaptive algorithm and Example 5. Left column plots show results for the surface gradient formulation (14), while the right column plots show results for the full gradient formulation (16).

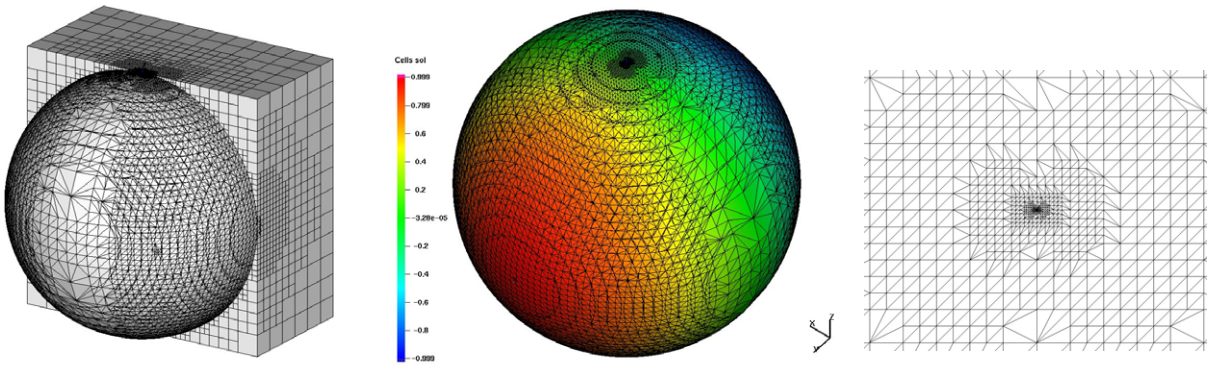

Fig. 8. Left and middle plots display the cutaway of the bulk and trace surface meshes in Example 5 with $\lambda = 0.6$ after 12 steps of refinement. The middle plot is shaded to reflect the numerical solution. The right picture shows the 20-x zoom in of the surface mesh near the north pole.

below is chosen to illustrate the ability of the trace FEM to handle these different cases by employing computational tools developed for volumetric finite elements: stabilization, error indicators, and layer fitted meshes. Numerical

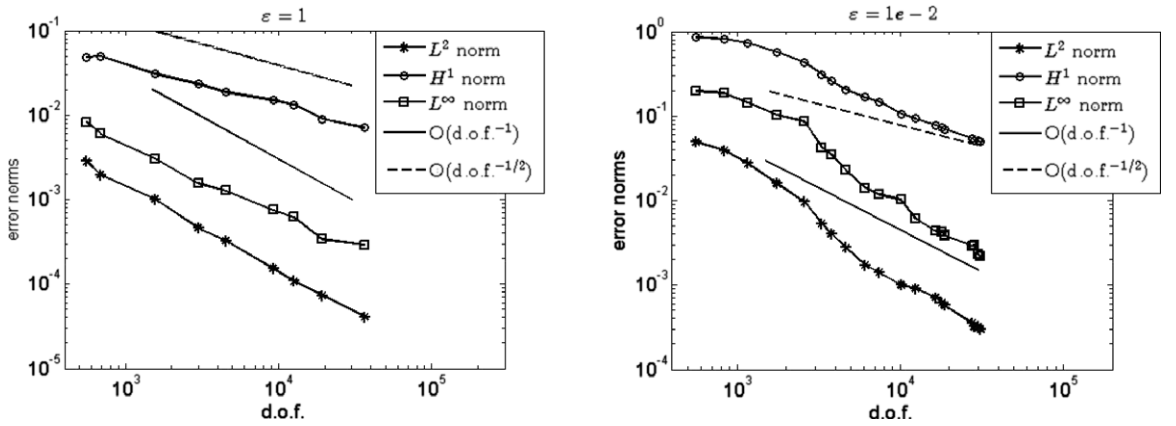

Fig. 9. Decrease of the error in the $L^2(\Gamma)$, $H^1(\Gamma)$ and $L^\infty(\Gamma)$ norms for the advection–diffusion problem from Example 6 with $Pe = 1$ (left) and $Pe = 100$ (right). The problem is solved on a sequence of adaptively refined grids.

results will show that the performance of such enhanced trace FEM appears to be similar to its volumetric counterparts applied to bulk advection–diffusion problems.

For the advection–diffusion problem we set weights α_r, α_e in the error indicator (62) dependent on the Peclet number as recommended in [41] for the planar advection–diffusion problem:

$$\alpha_r = \min\{\varepsilon^{-1}, h_{S_T}^{-2}\}, \qquad \alpha_e = \min\{\varepsilon^{-1}, h_{S_T}^{-1}\varepsilon^{-\frac{1}{2}}\}.$$

In experiments below geometry does not play an important role and so we set $\alpha_g = 0$.

Example 6. In this example, the stationary problem (5) is solved on the unit sphere Γ, with the velocity field

$$\mathbf{w}(\mathbf{x}) = \left(-x_2\sqrt{1-x_3^2}, x_1\sqrt{1-x_3^2}, 0\right)^T,$$

which is tangential to the sphere. We set $c = 1$ and consider $\varepsilon \in [10^{-6}, 1]$. Letting $W := \|\mathbf{w}\|_{L^\infty(\Gamma)}$ and $L = \mathrm{diam}(\Gamma)$, we compute the Peclet number as $Pe = \varepsilon^{-1}$.

For the exact solution to (5), we take the function

$$u(\mathbf{x}) = x_1x_2\arctan\left(\frac{2x_3}{\sqrt{\varepsilon}}\right).$$

The corresponding right-hand side function f is given by

$$f(\mathbf{x}) = \frac{12\varepsilon^{3/2}x_1x_2x_3}{\varepsilon + 4x_3^2} + \frac{16\varepsilon^{3/2}(1-x_3^2)x_1x_2x_3}{(\varepsilon+4x_3^2)^2} + (6\varepsilon x_1x_2 + \sqrt{x_1^2+x_2^2}(x_1^2-x_2^2))\arctan\left(\frac{2x_3}{\sqrt{\varepsilon}}\right) + u.$$

When ε gets smaller, a layer of the width $O(\varepsilon^{\frac{1}{2}})$ is forming in u along the equator of the sphere ($\{x_3 = 0\} \cap \Gamma$). The formation of characteristic internal layers of $O(\varepsilon^{\frac{1}{2}})$-width is typical for advection–diffusion problems.

In this paper, we consider equations posed on closed surfaces, therefore we are not treating parabolic or exponential boundary layers.

5.4.1. Lower Peclet number case

We consider Eq. (5) for $Pe \le 100$ to be non-singular perturbed. Hence, for this case of lower Peclet numbers, we expect the trace finite element to behave similar to the case of Laplace–Beltrami equations with smooth solution. We add no stabilization in this case and recover the expected $O(h^2)$ and $O(h)$ convergence rates on a sequence of uniformly refined grids in L^2 and H^2 surface norms, respectively (not shown). Fig. 9 shows the error reduction plots for $Pe = 1$ and $Pe = 100$ if a mesh adaptation is performed based on the error indicator (62). For $Pe = 100$, the error norms are approximately one order bigger than for $Pe = 1$, but in both cases the convergence curves demonstrate

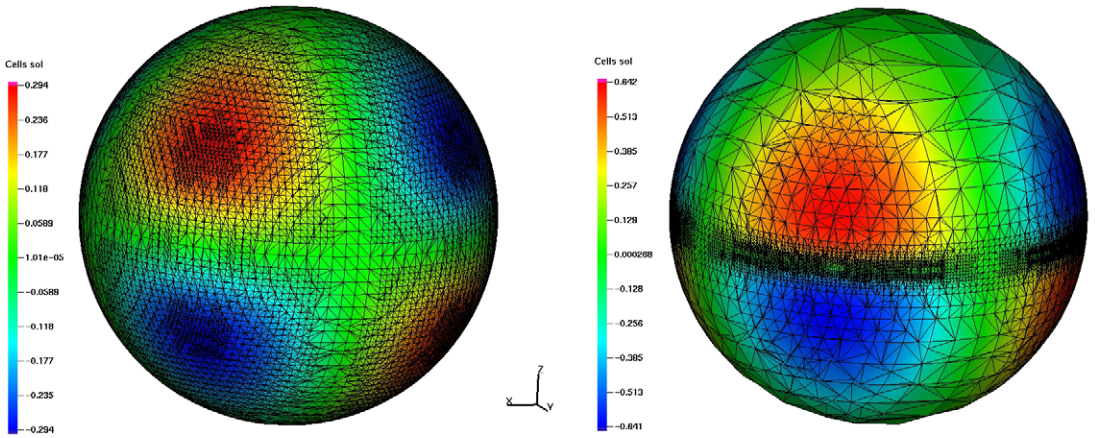

Fig. 10. The numerical solutions for the convection–diffusion problem from Example 6 with $Pe = 1$ (left) and $Pe = 100$ (right). The surface meshes are shown after 7 (left) and 9 (right) steps of adaptive refinement.

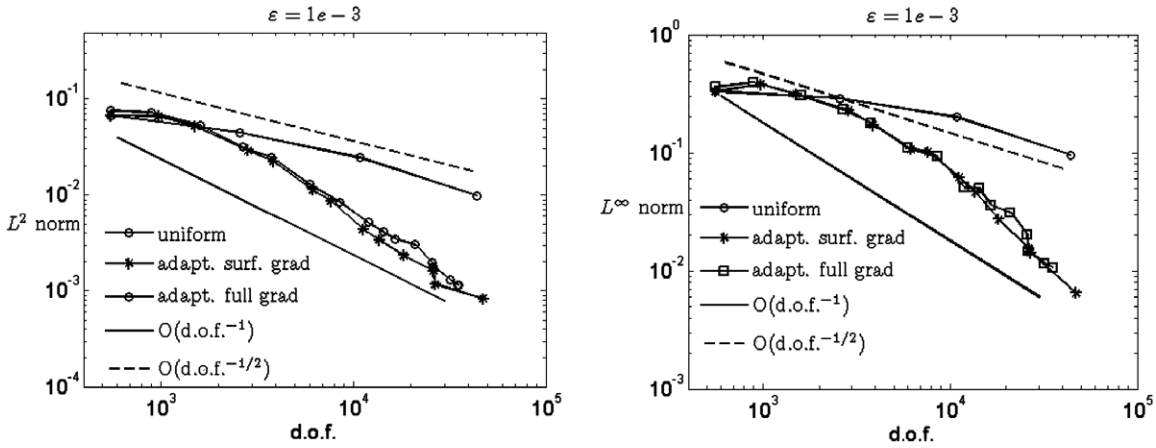

Fig. 11. Decrease of the error for the "surface gradient" and "full gradient" versions of the trace FEM for the advection–diffusion problem from Example 6 with $Pe = 10^3$. The error is measured in the $L^2(\Gamma_h)$ norm (left) and $L^\infty(\Gamma_h)$ norm (right). Both plots compare the error of the "surface gradient" and "full gradient" variants of the method on a sequence of adaptively refined grids with the error of the "surface gradient" variant on the sequence of uniformly refined meshes.

optimal reduction rates versus the number of active degrees of freedom. The numerical solutions and the surface meshes after several steps of adaptive refinement are displayed in Fig. 10. For $Pe = 100$, most of refinement happens closer to the equator of the sphere.

The results are shown for the trace finite element formulation with surface gradient (16). The results for the method with full gradient (16) were largely similar.

5.4.2. *Higher Peclet number case*

Now we consider Eq. (5) and $Pe \geq 10^3$. For the growing Peclet number, the problem becomes increasingly singular perturbed. For $Pe = 10^3$ the internal layer becomes pronounced. Now and in all further experiments in this section, we apply SUPG stabilized trace finite element method (17).

Already for $Pe = 10^3$ the uniform refinement does not lead to typical $O(h^2)$ convergence behavior (unless the mesh is sufficiently fine to resolve the boundary layer.) This is well seen from results shown in Fig. 11. The error decrease on uniformly refined grid is shown only for the "surface gradient" variant of the trace FEM (14), since the results with (16) were very similar. The adaptive refinement based on the indicator (62) leads, however, to the optimal error decrease with respect to the number of active d.o.f. These results are also demonstrated in Fig. 11. The "surface gradient" and "full gradient" variants show very close results.

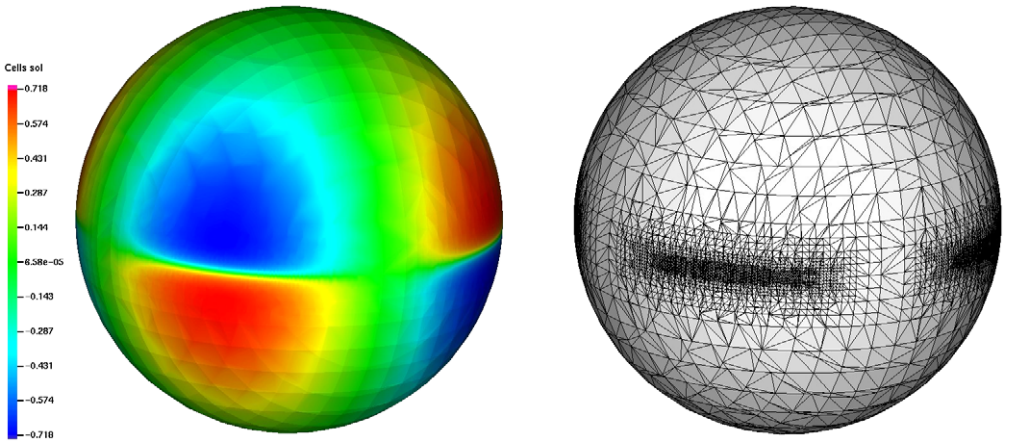

Fig. 12. Numerical solution and the mesh after 9 refinement steps for the convection–diffusion problem from Example 6 with $Pe = 10^3$.

Table 2
Convergence of numerical solutions to the advection–diffusion problem from Example 6, with $Pe = 10^4$, on a sequence of Shishkin meshes.

#d.o.f.	L^2-norm	Rate	H^1-norm	rate	L^∞-norm	Rate
10,356	4.870e−3		1.577e−0		6.725e−2	
22,830	1.428e−3	1.77	7.597e−1	1.05	1.718e−2	1.97
101,332	3.739e−4	1.93	3.761e−1	1.01	5.484e−3	1.65

The numerical solution computed after 9 refinement steps and the corresponding surface mesh are demonstrated in Fig. 12. The internal characteristic layer is well seen in the solution. The error indicator (62) enforces an aggressive refinement in the regions of the layer.

Further, we consider the same problem with the higher Peclet number equal to 10^4. This time, the adaptive refinement based on the error indicator was not found to produce optimal error reduction for the number of degrees of freedom up to 50,000. Hence, we consider this problem to be a good test case for layer fitted meshes. We choose *Shishkin meshes* as one of the best studied class of meshes for singular-perturbed volumetric or planar problems. Shishkin meshes require an a priori knowledge of where a layer occurs and provide optimal convergence with respect to the total number of degrees of freedom [42].

Let N be the total number of nodal degrees of freedom available to discretize a singular-perturbed convection–diffusion problem. Assume that the solution to the problem has only an internal characteristic layer. Then to build a Shishkin mesh one defines a narrow band of width $O(\sqrt{\varepsilon}\ln N)$ around the layer and considers a mesh which is uniform inside and outside the band and contains $O(N)$ nodes in the interior of the narrow band as well as in the rest of computational domain (see, e.g., [42] for accurate definitions). We extend this construction to the case of octree bulk meshes and the singular-perturbed problem posed on a surface as follows. We build an initial octree mesh such that $h_{\min} = 1/128$ was the size of cubes inside the strip $|x_3| \leq 1/64$ (this defines our "narrow band" containing the layer). In the rest of the bulk domain, the grid was aggressively coarsened up to $h_{\max} = 1/4$. The resulted number of active degrees of freedom for this initial mesh was 10,356. Further, the mesh was uniformly refined two times, leading to layer fitted meshes with 22,830 and 101,332 active degrees of freedom. We note two deviations of our construction from the classical notion of a Shishkin mesh: (i) We do not re-balance the mesh to account for the logarithmic factor in the width of a narrow band of a canonical Shishkin mesh; (ii) The mesh outside our narrow band is not completely uniform due to a transition region, which is necessary to keep the octree balanced (two neighboring cubes may differ in size at most by a factor of 2).

Fig. 13 shows the numerical solution computed on the finest surface Shishkin mesh. Note that the internal layer is sharp and resolved. We observe no numerical oscillations in a vicinity of the layer. Table 2 presents the norms of the finite element error on the sequence of the layer fitted meshes and corresponding convergence factors.

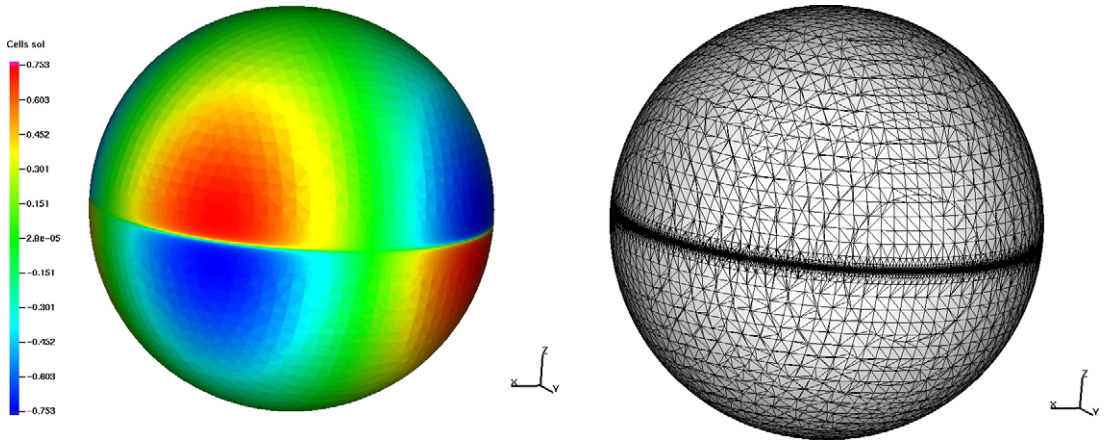

Fig. 13. Numerical solution and the Shishkin mesh for the advection–diffusion problem from Example 6 with the $Pe = 10^4$.

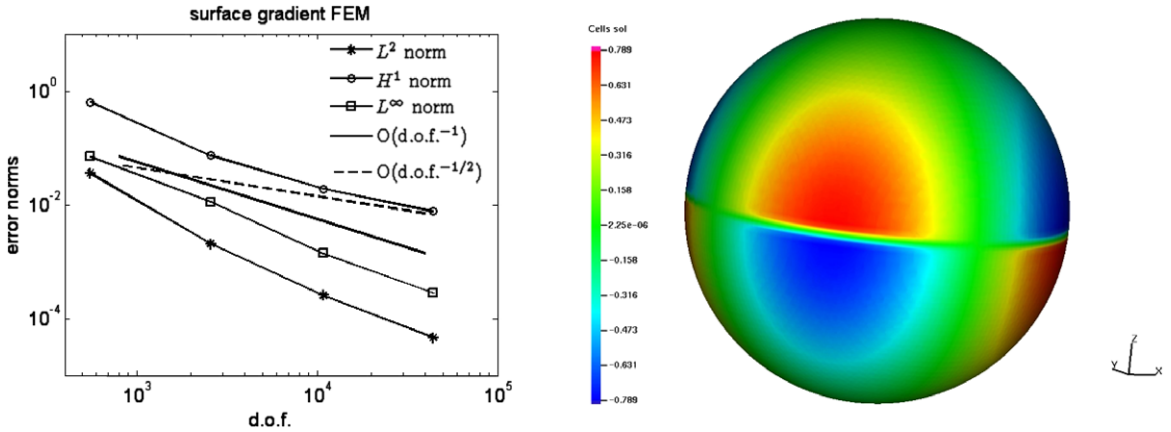

Fig. 14. Left: Decrease of the error in the $L^2(\Gamma_{ext})$, $H^1(\Gamma_{ext})$ and $L^\infty(\Gamma_{ext})$ norms for the advection–diffusion problem from Example 6 with $Pe = 10^6$. Γ_{ext} is a part of the domain well separated from the internal layer. The problem was solved on a sequence of uniformly refined meshes. Right: Numerical solution for the advection–diffusion problem from Example 6 with $Pe = 10^6$ on a uniformly refined mesh. The internal layer is not resolved and clearly smeared over few mesh sizes. No spurious oscillations can be noted.

Finally, we solve the same problem, but now with $\varepsilon = 10^{-6}$, leading to $Pe = 10^6$. The width of the internal layer is $O(\varepsilon^{\frac{1}{2}})$, and we are not attempting to resolve it with a layer fitted mesh. Instead we solve the problem on a sequence of uniformly refined grids. Since we used the SUPG stabilized formulation of the finite element method, we can expect that similar to a planar or a volumetric cases the layer would be smeared, numerical oscillation damped, and finite element solution converges to the exact one outside the layer. This is exactly what we observed for our trace finite element method. Thus, Fig. 14 demonstrates the computed solution as well as the finite element error decrease in a part of the domain separated from the layer: All norms in Fig. 14 (left) were computed over part of the sphere $\Gamma_{ext} := \{\mathbf{x} \in \Gamma \,:\, |x_3| > 0.3\}$.

6. Conclusions

We studied a trace finite element method for partial differential equations posed on hypersurfaces in $\mathbb{R}^3$. An extension to curves in $\mathbb{R}^2$ is straightforward. The paper demonstrates that using such standard computational tools as cartesian octree grids, a marching cubes method, and trilinear bulk finite elements leads to a second order accurate method with a number of attractive features: The mesh is unfitted to a surface; One uses standard finite element tools without any extension of equation from the surface to bulk domain; The method works for surfaces defined implicitly, parametrization of a surface is *not* required; The number of active d.o.f. is optimal and comparable to methods in

which Γ is meshed directly; Optimal order of convergence in H^1 and L^2 norms is proved for quasi-uniform bulk grids. Moreover, due to the natural connection to bulk elements, many tools and techniques well established for "usual" discretizations carry over to the surface case. In this paper, we experimented with several such techniques: adaptivity based on an error indicator, SUPG stabilization for transport dominant equations, and layer fitted meshes. Numerical analysis supports experimental observations. In forthcoming papers we plan to extend the adaptive octree trace finite element method to PDEs defined on evolving surfaces and to apply it for the simulation of flow and transport in fractured porous media.

Acknowledgments

This work has been supported by RFBR through the grants 14-01-00731, 14-01-00830 and by National Science Foundation through the Division of Mathematical Sciences grant 1315993.

References

[1] W.W. Mullins, Mass transport at interfaces in single component system, Metall. Mater. Trans. 26 (1995) 1917–1925.
[2] C.M. Elliott, B. Stinner, Modeling and computation of two phase geometric biomembranes using surface finite elements, J. Comput. Phys. 229 (2010) 6585–6612.
[3] S. Gross, A. Reusken, Numerical Methods for Two-phase Incompressible Flows, vol. 40, Springer-Verlag, 2011.
[4] U. Diewald, T. Preufer, M. Rumpf, Anisotropic diffusion in vector field visualization on Euclidean domains and surfaces, IEEE Trans. Vis. Comput. Graph. 6 (2000) 139–149.
[5] G. Turk, Generating textures on arbitrary surfaces using reaction–diffusion, Comput. Graph. 25 (1991) 289–298.
[6] A. Toga, Brain Warping, Academic Press, New York, 1998.
[7] D. Halpern, O. Jensen, J. Grotberg, A theoretical study of surfactant and liquid delivery into the lung, J. Appl. Physiol. 85 (1998) 333–352.
[8] G. Dziuk, Finite elements for the Beltrami operator on arbitrary surfaces, in: S. Hildebrandt, R. Leis (Eds.), Partial Differential Equations and Calculus of Variations, in: Lecture Notes in Mathematics, vol. 1357, Springer, Berlin, 1988, pp. 142–155.
[9] M. Bertalmio, L. Cheng, S. Osher, G. Sapiro, Variational problems and partial differential equations on implicit surfaces: The framework and examples in image processing and pattern formation, J. Comput. Phys. 174 (2001) 759–780.
[10] K. Deckelnick, C.M. Elliott, T. Ranner, Unfitted finite element methods using bulk meshes for surface partial differential equations, arXiv preprint arXiv:1312.2905.
[11] M. Olshanskii, D. Safin, A narrow-band unfitted finite element method for elliptic pdes posed on surfaces, arXiv preprint arXiv:1401.7697 Math. Comp., in press.
[12] G. Dziuk, C.M. Elliott, Finite element methods for surface PDEs, Acta Numer. (2013) 289–396.
[13] M. Olshanskii, A. Reusken, J. Grande, A finite element method for elliptic equations on surfaces, SIAM J. Numer. Anal. 47 (2009) 3339–3358.
[14] M. Olshanskii, A. Reusken, A finite element method for surface PDEs: Matrix properties, Numer. Math. 114 (2010) 491–520.
[15] A. Bonito, R. Nochetto, M. Pauletti, Dynamics of biomembranes: effect of the bulk fluid, Math. Model. Nat. Phenom. 6 (2011) 25–43.
[16] C.M. Elliott, T. Ranner, Finite element analysis for coupled bulk-surface partial differential equation, IMA J. Numer. Anal. 33 (2013) 377–402.
[17] J. Grande, Eulerian finite element methods for parabolic equations on moving surfaces, SIAM J. Sci. Comput. 36 (2014) 248–271.
[18] P. Hansbo, M.G. Larson, S. Zahedi, Characteristic Cut Finite Element Methods for Convection–Diffusion Problems on Time Dependent Surfaces, Tech. Rep., Uppsala University, 2013, April.
[19] M. Olshanskii, A. Reusken, X. Xu, An eulerian space–time finite element method for diffusion problems on evolving surfaces, SIAM J. Numer. Anal. 52 (2014) 1354–1377.
[20] M. Olshanskii, A. Reusken, Error analysis of a space–time finite element method for solving PDEs on evolving surfaces, SIAM J. Numer. Anal. 52 (2014) 2092–2120.
[21] E. Burman, P. Hansbo, M.G. Larson, S. Zahedi, Cut finite element methods for coupled bulk-surface problems, arXiv preprint arXiv:1403.6580.
[22] S. Gross, M.A. Olshanskii, A. Reusken, A trace finite element method for a class of coupled bulk-interface transport problems, arXiv preprint arXiv:1406.7694.
[23] M. Olshanskii, A. Reusken, X. Xu, A stabilized finite element method for advection–diffusion equations on surfaces, IMA J Numer. Anal. 34 (2014) 732–758.
[24] A. Reusken, Analysis of trace finite element methods for surface partial differential equations, IGPM RWTH Aachen preprint 387.
[25] A. Demlow, M. Olshanskii, An adaptive surface finite element method based on volume meshes, SIAM J. Numer. Anal. 50 (2012) 1624–1647.
[26] E. Burman, P. Hansbo, M.G. Larson, A stabilized cut finite element method for partial differential equations on surfaces: The Laplace–Beltrami operator, Comput. Methods Appl. Mech. Engrg. 285 (2015) 188–207.
[27] F. Losasso, F. Gibou, R. Fedkiw, Simulating water and smoke with an octree data structure, ACM Trans. Graph. (TOG) 23 (3) (2004) 495–514.
[28] D. Meagher, Geometric modeling using octree encoding, Comput. Graph. Image Process. 19 (1982) 129–147.
[29] R. Szeliski, Rapid octree construction from image sequences, CVGIP: Image Underst. 58 (1993) 23–32.
[30] S. Popinet, An accurate adaptive solver for surface-tension-driven interfacial flows, J. Comput. Phys. 228 (2009) 5838–5866.
[31] J. Strain, Tree methods for moving interfaces, J. Comput. Phys. 151 (1999) 616–648.
[32] K.D. Nikitin, M.A. Olshanskii, K.M. Terekhov, Y.V. Vassilevski, A numerical method for the simulation of free surface flows of viscoplastic fluid in 3D, J. Comput. Math. 29 (2011) 605–622.

[33] W. Bangerth, R. Hartmann, G. Kanschat, DEAL II – a general-purpose object-oriented finite element library, ACM Trans. Math. Software (TOMS) 33 (4).
[34] S. Popinet, Gerris: a tree-based adaptive solver for the incompressible Euler equations in complex geometries, J. Comput. Phys. 190 (2003) 572–600.
[35] W. Lorensen, H. Cline, Marching cubes: A high resolution 3d surface construction algorithm, ACM SIGGRAPH 21 (4) (1987) 189–207.
[36] T. Aubin, Nonlinear Analysis on Manifolds, Monge–Ampere Equations, Vol. 252, Springer, 1982.
[37] C.-C. Ho, F.-C. Wu, B.-Y. Chen, Y.-Y. Chuang, M. Ouhyoung, Cubical marching squares: Adaptive feature preserving surface extraction from volume data, in: EUROGRAPHICS 2005 / M. Alexa and J. Marks (Guest Editors) 24 (3).
[38] A. Demlow, G. Dziuk, An adaptive finite element method for the Laplace–Beltrami operator on implicitly defined surfaces, SIAM J. Numer. Anal. 45 (2007) 421–442.
[39] A. Hansbo, P. Hansbo, M.G. Larson, A finite element method on composite grids based on Nitsche's method, ESAIM Math. Model. Numer. Anal. 37 (2003) 495–514.
[40] V. Heuveline, F. Schieweck, H1-interpolation on quadrilateral and hexahedral meshes with hanging nodes, Computing 80 (3) (2007) 203–220.
[41] R. Verfürth, A posteriori error estimators for convection–diffusion equations, Numer. Math. 80 (4) (1998) 641–663.
[42] G. Shishkin, Discrete Approximation of Singularly Perturbed Elliptic and Parabolic Equations, Tech. Rep., vol. 269, Russian Academy of Sciences, Ural Section, Ekaterinburg, 1992.